

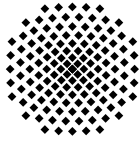
Diplomarbeit

# CO<sub>2</sub> Storage into Dipped Saline Aquifers Including Ambient Water Flow

Submitted by  
Klaus Mosthaf  
Matrikelnummer 2040550

Stuttgart, July 29th, 2007

Examiners: Prof. Dr.-Ing. Rainer Helmig, Dr.-Ing. Holger Class  
Supervisor: Dipl.-Ing. Andreas Kopp, M.Sc



## Diplomarbeit

Klaus Mosthaf  
Matr.Nr. 2040550

### **CO<sub>2</sub> Storage into Dipped Saline Aquifers Including Ambient Water Flow.**

Concerns on man-made climate change due to high CO<sub>2</sub> concentrations in the atmosphere have led to the idea of storing CO<sub>2</sub> in geologic formations. Suitable reservoirs are to be found that are capable of storing CO<sub>2</sub> over long periods of time safely. Classical options often include to store CO<sub>2</sub> in deep saline formations or in depleted oil and gas reservoirs, use CO<sub>2</sub> for enhanced oil and gas recovery (EGR) or for enhanced coal bed methane recovery (ECBM). Ideally the caprock has a anticlinal structure to stop the CO<sub>2</sub> from rising further upwards by hydrodynamic trapping. Nevertheless if conditions are favourable a storage below a dipped caprock seems possible. Necessary conditions are a strong background flow that forces the CO<sub>2</sub> to migrate in deeper regions and solute rapidly in brine or a very low reservoir permeability causing very slow CO<sub>2</sub> movement. These options are to be investigated here.

Principle investigations have to be performed to gain insight in the system behaviour. Furtheron the knowledge is to be used in the development of dimensionless groups, describing the system behaviour. Application example is a shallow reservoir in northern Germany below a caprock with a dipping angle of approx. 3%.

The storage of CO<sub>2</sub> in sub- or supercritical state in geological formations can be considered as a multiphase multicomponent system in a porous medium. The multiphase system is formed by a solid matrix, the rock, and two fluid phases, the gaseous and the liquid. The brine-rich phase represents the liquid phase and the CO<sub>2</sub>-rich phase the gaseous. In the context of this work the program system MUFTE-UG (Multiphase Flow, Transport and Energy, Unstructured Grids) developed by LH<sup>2</sup> will be used for numerical simulation and analysis.

**In detail, the following tasks have to be fulfilled:**

- Perform numerical simulations on CO<sub>2</sub> storage in dipped aquifers using MUFTE-UG. Simulations shall be conducted in 2 dimensional space. Necessary steps include grid construction, definition of boundary conditions, define parameter settings like permeability, porosity etc.
- Include background water flow in the studies and show its influence.
- Find dimensionless groups to describe CO<sub>2</sub> plume shape and evolution behaviour in the above mentioned cases.
- Build a numerical model of a complex 3-dimensional application case. Necessary steps include 3D model building in CAD and grid construction in ICEM CFD, definition of boundary conditions and incorporation of data given by project partner. The data given can include spatial information on caprock geometry and heterogeneous permeability distribution.

The study shall be documented in a report using  $\text{\LaTeX}$  and summarised in an oral presentation.

Literature:

D.J. Wood, L.W. Lake, R.T. Jones and V. Nunez *A Screening Model for CO<sub>2</sub> Flooding and Storage in Gulf Coast Reservoirs Based on Dimensionless Groups*, 2006.

J. vanLookeren *Calculation Methods for Linear and Radial Steam Flow in Oil Reservoirs*, 1983.

(Prof. Dr.-Ing. R. Helmig)

**Examiner:** Prof. Dr.-Ing. Rainer Helmig and Dr.-Ing. Holger Class  
**Supervisor:** Dipl.-Ing. Andreas Kopp, M.Sc.  
**Start:** 29.01.2007  
**End:** 29.07.2007

## **Author's Statement**

I herewith certify that I created this Diploma thesis independently, and that all used sources are duly referenced, if not wished differently by the contributor.

(Klaus Mosthaf, August 2007)

# Contents

<b>1</b>	<b>Introduction</b>	<b>1</b>
1.1	The Carbon Dioxide Problem - The Idea of CO <sub>2</sub> Sequestration . . . . .	1
1.1.1	The Carbon Dioxide Problem . . . . .	1
1.1.2	Current Work . . . . .	3
1.1.3	Aims of this Thesis . . . . .	4
1.1.4	Structure of this Thesis . . . . .	5
<b>2</b>	<b>Physical Properties</b>	<b>6</b>
2.1	Properties of CO <sub>2</sub> . . . . .	6
2.1.1	Density and Dynamic Viscosity . . . . .	7
2.1.2	Enthalpy . . . . .	10
2.2	Properties of Brine . . . . .	10
2.2.1	Density and Dynamic Viscosity . . . . .	10
2.2.2	Enthalpy . . . . .	11
2.3	Important Processes . . . . .	12
2.3.1	Solubility of the Fluids . . . . .	12
2.3.2	Advection and Hydrodynamic Dispersion . . . . .	13
2.3.3	Capillary Pressure . . . . .	13
2.3.4	Relative Permeability . . . . .	14
2.3.5	Hysteresis . . . . .	14
2.4	Criteria for Storage Reservoirs and Trapping Mechanisms . . . . .	16
2.4.1	Trapping Mechanisms . . . . .	16
<b>3</b>	<b>Model Concept</b>	<b>18</b>
3.1	Fundamental Terms . . . . .	18
3.1.1	Phases and Components . . . . .	18
3.1.2	Representative Elementary Volume, REV . . . . .	19
3.2	Conceptual Model . . . . .	20
3.3	Mathematical and Numerical Model . . . . .	20
3.3.1	Governing Equations . . . . .	20
3.3.2	Discretization Scheme . . . . .	22
3.3.3	Primary and Secondary Variables . . . . .	22

<b>4</b>	<b>2D Simulations</b>	<b>25</b>
4.1	General Setup . . . . .	25
4.1.1	Description of the Used Mesh . . . . .	26
4.2	Initial Values and Boundary Conditions . . . . .	26
4.3	Description of the Reference Model . . . . .	28
4.4	Determination of the Flow Direction . . . . .	29
4.5	Subdivision of the Process into two Stages . . . . .	34
4.5.1	Stage I: Free Movement . . . . .	34
4.5.2	Stage II: Migration Along the Cap Rock . . . . .	37
4.6	Mass Distribution in the Aquifer . . . . .	39
4.7	Parameter Variation . . . . .	39
4.7.1	Variation of the Aquifer Depth . . . . .	40
4.7.2	Variation of the Dip Angle . . . . .	43
4.7.3	Variation of the CO <sub>2</sub> Injection Pressure . . . . .	45
4.7.4	Variation of the Ambient Formation Water Flow . . . . .	48
4.7.5	Variation of the Intrinsic Permeability . . . . .	50
4.8	Results . . . . .	51
<b>5</b>	<b>3D Simulations</b>	<b>55</b>
5.1	Aquifer Parameters and Simulation Setup . . . . .	55
5.1.1	Underlying Data . . . . .	56
5.1.2	Boundary Conditions . . . . .	58
5.1.3	Aquifer and Fluid Properties . . . . .	59
5.2	Description of the Different Model Runs . . . . .	60
5.2.1	Case 1: 1 Mtons per Year, Normal Depth . . . . .	60
5.2.2	Case 2: 2.3 Mtons per Year, Normal Depth . . . . .	61
5.2.3	Case 3: 0.5 Mtons per Year, Normal Depth . . . . .	62
5.2.4	Case 4: 0.1 Mtons per Year, Normal Depth . . . . .	62
5.2.5	Case 5: 1 Mtons per Year in a Supercritical State . . . . .	62
5.2.6	Case 6: Two Different Permeability Zones . . . . .	63
5.3	After the Injection is Turned off . . . . .	64
5.3.1	Behavior After the Injection is Turned off . . . . .	64
5.4	Not Examined Parts and Risks . . . . .	68
5.5	Chances and Possibilities . . . . .	70
<b>6</b>	<b>Summary and Outlook</b>	<b>74</b>
6.1	Conclusions and Outlook . . . . .	74

# List of Figures

1.1	Increase of the carbon dioxide concentrations in the atmosphere . . . . .	2
1.2	Different storage options for CO <sub>2</sub> . . . . .	3
2.1	Phase diagram of CO <sub>2</sub> . . . . .	7
2.2	CO <sub>2</sub> switching from two phases to supercritical . . . . .	8
2.3	Density and viscosity of CO <sub>2</sub> in correlation to pressure . . . . .	8
2.4	Density and dynamic viscosity of CO <sub>2</sub> over depth . . . . .	9
2.5	Enthalpy of carbon dioxide . . . . .	10
2.6	Density and dynamic viscosity of brine . . . . .	11
2.7	Enthalpy of brine . . . . .	12
2.8	Solubility of CO <sub>2</sub> - pressure diagram . . . . .	13
3.1	Two-phase two-component model concept . . . . .	20
4.1	Simulation setup . . . . .	25
4.2	2D boundary conditions . . . . .	26
4.3	Saturations of the reference case at three different points in time . . . . .	30
4.4	Resulting pressure gradient in X-direction . . . . .	32
4.5	Components of the gravity vector . . . . .	34
4.6	Mass flow over time . . . . .	37
4.7	Depth of 350 meters and 1500 meters . . . . .	41
4.8	Dimensionless numbers and mass ratio with depth . . . . .	42
4.9	Dip angle of 0° and 20° . . . . .	43
4.10	Dimensionless numbers and mass ratio with different dip angles . . . . .	44
4.11	Injection Pressure of 2E5 Pa and 10E5 Pa . . . . .	45
4.12	Dimensionless numbers and mass ratio with different injection pressures . . . . .	46
4.13	Mass flow with different injection pressures . . . . .	47
4.14	No formation water flow and high flow rate . . . . .	48
4.15	Pressure number and mass ratio with flow pressure . . . . .	49
4.16	Low and high permeability . . . . .	50
4.17	Dimensionless numbers and mass ratio with different permeabilities . . . . .	51
4.18	Overview of the used values . . . . .	53
4.19	Overview of the calculated numbers . . . . .	54
5.1	Aquifer geometry . . . . .	56

---

5.2	Top view on the whole domain . . . . .	57
5.3	Formation water stream traces . . . . .	58
5.4	Stream traces of the water phase . . . . .	61
5.5	Saturation profile when the cap rock is reached . . . . .	62
5.6	Two permeabilities, top view . . . . .	63
5.7	Two different permeabilities . . . . .	64
5.8	Behavior after stopping the injection . . . . .	65
5.9	Same mass in the system with different injection rates . . . . .	66
5.10	Dissolution behavior . . . . .	69
5.11	Injection of 1 Mt/year . . . . .	71
5.12	Injection of 0.1 Mt/year . . . . .	72
5.13	Injection in a supercritical state . . . . .	73

# List of Tables

2.1	Brooks-Corey parameters . . . . .	15
3.1	Adaptive choice of primary variables . . . . .	23
4.1	Constant parameters of the 2D simulations . . . . .	28
4.2	Parameters used for the reference case . . . . .	29
4.3	Estimation of the flow direction . . . . .	33
5.1	Constant parameters of the 3D simulations . . . . .	59
5.2	Brooks-Corey parameters . . . . .	59
5.3	Overview of simulated cases . . . . .	60

# Nomenclature

Subscript	Definition
$\alpha$	Phase
$w$	Water phase
$CO_2 / n$	CO <sub>2</sub> phase

Superscript	Definition
$\kappa$	Component
$w$	Water component
$CO_2$	CO <sub>2</sub> component

Symbol	Unit	Definition
$S_\alpha$	–	Saturation of phase $\alpha$
$X_\alpha^\kappa$	$kg/kg$	Mass fraction of $\kappa$ in $\alpha$
$k_{r,\alpha}$	–	Relative permeability of phase $\alpha$
$p_\alpha$	$Pa$	Phase pressure
$p_c$	$Pa$	Capillary pressure
$p_{inj}$	$Pa$	Injection pressure
$p_{flow}$	$Pa$	Pressure of the water flow
$h$	$m$	Piezometric head
$z$	$m$	Vertical coordinate
$H$	$J$	Enthalpy
$h$	$J/kg$	Specific Enthalpy
$U$	$J$	Internal energy
$u$	$J/kg$	Specific internal energy
$V$	$m^3/kg$	Volume
$v_\alpha$	$m/s$	Velocity of phase $\alpha$
$m$	$kg$	Mass
$\dot{m}$	$kg/s$	Mass flow
$T$	$K$	Temperature
$c$	$J/(kgK)$	Specific heat capacity
$d$	$m$	Pore diameter
$\mathbf{g}$	$m/s^2$	Gravity vector
$\mathbf{K}$	$m^2$	Intrinsic permeability tensor

Symbol	Unit	Definition
$K_{eff}$	$m^2$	Calculated effective permeability
$Gr$	—	Gravity number
$Pr$	—	Pressure number
$A_{LD}$	—	Van-Lookeren number
$\alpha$	$^\circ$	Dip angle of the aquifer
$\phi$	—	Porosity
$\rho$	$kg/m^3$	Density
$\mu$	$kg/(m \cdot s)$	Dynamic viscosity
$\lambda_{pm}$	$W/(mK)$	Heat conductivity of the porous medium
$\sigma$	$N/m$	Surface tension

# Chapter 1

## Introduction

### 1.1 The Carbon Dioxide Problem - The Idea of CO<sub>2</sub> Sequestration

#### 1.1.1 The Carbon Dioxide Problem

After the release of the latest United Nations Intergovernmental Panel on Climate Change (IPCC) report [15] about the global warming problem it is getting more and more clear that the emissions of greenhouse gases have to be reduced. Carbon dioxide (CO<sub>2</sub>) was identified to be a main contributor to climate change. It accumulates in the atmosphere, where it promotes global warming by enhancing the greenhouse effect. The rise of the carbon dioxide concentration within the atmosphere in the last decades since the industrialization is drastic. It is depicted in figure 1.1.

One of the main producers of this gas are power plants with combustion of fossil fuels like coal, natural gas, petroleum or biomass. The major part of energy (in Germany more than 50 per cent) is currently produced in coal plants, which are fired with anthracite and lignite. In 2006, the incineration of coal produced 325 million tons of carbon dioxide in Germany [2], which were emitted to the atmosphere. Furthermore, in many other countries, the energy mix is even more dominated by the combustion of fossil fuels, especially coal. In China for example, two 500 MW coal plants are built each week in order to meet the fast-growing demand [1]. In one 500 MW coal plant, approximately two to five million tons of carbon dioxide are emitted per year [1].

Coal has the advantage, that it is in many countries still available in large amounts and has comparably low costs for the energy generation. Apparently, coal will continue to play an important role in the future as well [1], because other non-renewable resources (even uranium) will run out before the coal reserves, and the renewable energy sources are up to now not able to replace them and to grant a secure energy supply.

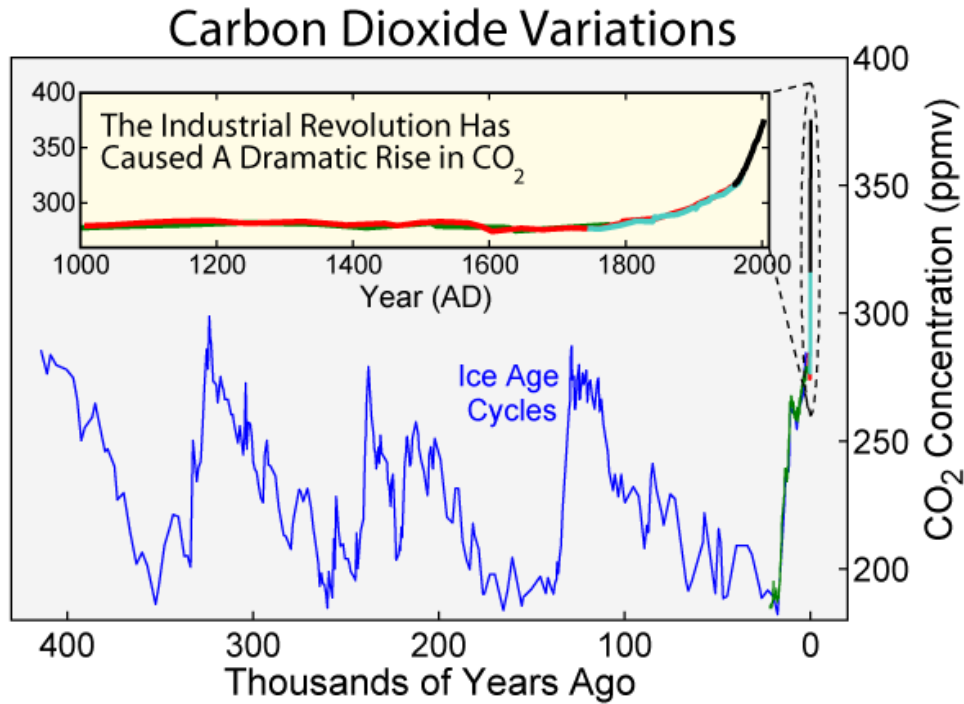


Figure 1.1: Increase of the carbon dioxide concentrations in the atmosphere in the last 400 thousand years. The natural fluctuations of the concentration in the atmosphere are shown. Since the beginning of the industrialization in the 19th Century, the concentration have been showing a strong upwards trend. Source: [www.globalwarmingart.com](http://www.globalwarmingart.com), based on data from the U.S. Department of Energy.

The issue with the combustion of fossil fuels is that the coal compounds (natural gas, crude oil or coal) are taken out of the subsurface and are then transformed to a great part into carbon dioxide. This is emitted into the atmosphere. Naturally, there were about 280 parts per million CO<sub>2</sub> in the lower atmosphere, which is part of a huge carbon circle and also varies over time. However, the CO<sub>2</sub> that comes out of fossil fuel combustion is not part of this circle but additionally produced. This is increasing the carbon dioxide concentration in the atmosphere and has a negative impact on the climate and subsequently on nature and mankind. In 2006, the atmospheric CO<sub>2</sub> concentrations amounted to 380 parts per million (V) with a clear upwards trend.

However, much energy is needed and no better way to produce it is available yet. So the evolving CO<sub>2</sub> emissions from using fossil fuels have to be reduced or prevented from reaching the atmosphere. A promising idea, which shall be discussed further here, is to separate the carbon dioxide from the emissions of stationary point sources such as power plants or factories and to pump the purified and concentrated fluid into suitable storage sites in the subsurface. It shall be permanently stored there. Figure 1.2 gives an overview of the different storage possibilities. These can be deep saline

aquifers, former natural gas and oil deposits or unminable coal beds. Moreover, the idea of storing carbon dioxide into the deep sea exists.

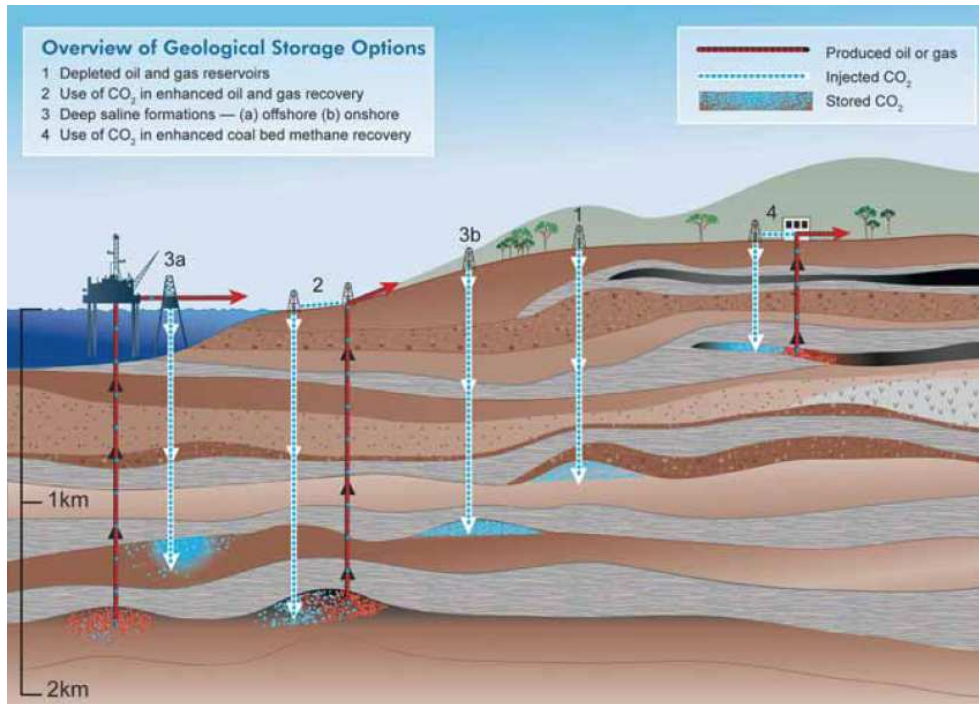


Figure 1.2: Different storage options for CO<sub>2</sub>. Source: Intergovernmental Panel on Climate Change, [www.ipcc.ch](http://www.ipcc.ch)

### 1.1.2 Current Work

Currently, there are several projects running in the field of carbon dioxide sequestration. In 1996, the Sleipner project in Norway was started. There are approximately one million tons of CO<sub>2</sub> per year pumped into a huge saline sandstone aquifer called Utsira formation, which is situated under the North Sea in a depth of 1000 meters. The CO<sub>2</sub> was separated from the extraction and purification process of natural gas from the offshore gas field called Sleipner in North Sea. Up to now, the results indicate that save storage of CO<sub>2</sub> under a suitable cap rock is possible. The injected carbon dioxide was monitored successfully by seismic surveying in a related project called SACS, which aims at finding suitable monitoring methods.

Another important project is currently performed near the town Ketzin west of Berlin, where CO<sub>2</sub> is injected into a deep saline formation. It is the first European on-shore CO<sub>2</sub> sequestration project. This showcase shall help to get a better understanding of the sequestration and monitoring processes.

Besides, CO<sub>2</sub> has been pumped into depleted oil reservoirs in the context of enhanced oil recovery (EOR) for several years. There, its function is primarily to increase the feed rates of the oil production and to extend the lifetime of oil reservoirs. But, as a welcome side effect, the injected CO<sub>2</sub> is sequestered and kept away from the atmosphere. Enhanced oil/gas recovery is probably the most economic way of storing CO<sub>2</sub> in the subsurface. The used technology in the case of EOR is well-known and the same as in sole CO<sub>2</sub> storage processes. An example for a running EOR project including CO<sub>2</sub> sequestration can be found at the Weyburn oil fields in south Canada. It was stated in the year 2000. An amount of 20 million tons is foreseen to be permanently pumped into the oil reservoirs within 30 years and permanently stored there.

The processes, that occur in CO<sub>2</sub> sequestration are very complex with many different parameters influencing the behavior of the injected CO<sub>2</sub>. Moreover, field experiments are very expensive and include certain risks. The processes of CO<sub>2</sub> storage can be described by different highly non-linear equations and complex partial differential equations. For those, the analytical solution of such problems is often difficult or impossible to obtain. To get despite this an impression what is going on in such a process, the help of numerical simulations is required.

### 1.1.3 Aims of this Thesis

In this thesis, the storage of carbon dioxide into saline aquifers or aquifer parts with a dip angle and ambient water flow in down dip direction shall be examined and discussed with the help of numerical models. It will be determined, how different parameters like dip angle, injection pressure or injection depth influence the propagation behavior of the injected CO<sub>2</sub>. Different occurring processes will be examined and explained. The dimensionless Van-Lookeren number, which describes the ratio of buoyancy forces to viscous forces, will be used to characterize the propagation behavior. Moreover, rough estimations for the expected direction of the propagation will be presented. Finally, recommendations for the use of such aquifers and for the suitability for carbon dioxide storage will be made.

The idea behind an injection into a dipped aquifer with ambient water flow in down dip direction is

- to generate a preferably big contact surface for a better dissolution of the carbon dioxide in the brine
- to maximize residual CO<sub>2</sub> trapping through a long migration distance
- to save drilling costs by setting a bore hole up dip a suitable storage site
- to enhance storage safety with the help of the formation water flow, which enforces the downwards movement and acts against buoyancy

Moreover, many reservoirs are not horizontal but have a certain dip angle. Therefore, it is interesting to see how this influences the propagation behavior.

#### 1.1.4 Structure of this Thesis

The first part of the thesis gives a brief introduction to CO<sub>2</sub>-sequestration, the underlying reasons and the dominating physical properties and processes. These are further explored with the help of numerical models. The numerical and mathematical model concepts that are used for the simulations are explained. Then, a reference model is set up and presented. The process of injecting CO<sub>2</sub> into a dipped aquifer, where formation water is flowing down dip, is very complex and includes a bunch of parameters that have an influence on the flow and propagation behavior. Several two-dimensional models are used then to simulate CO<sub>2</sub> sequestration in such aquifers with different parameters as the reference model like aquifer depth, dip angle or water flow. With the help of these simulations the influence of these parameters on the propagation behavior of the injected CO<sub>2</sub> is examined. Two dimensionless numbers are applied to describe the influence of these parameters on the shape of the evolving plume.

In the second part, real world data is used to build up a three-dimensional numerical model of a dipped saline aquifer at a prospective site. Due to high recharge rates from upstream there is a formation water flow down dip the aquifer. The behavior of CO<sub>2</sub>, which is injected into this flow is examined and explained with the help of the observations that were made in the two-dimensional models. Statements about the suitability of the given aquifer and different possibilities for long-term storage are made. Various parameter setups are tested and and evaluated.

# Chapter 2

## Physical Properties

The sequestration of carbon dioxide into saline aquifers includes various parameters and physical processes that influence the system behavior and that are important for accurate simulations. For the development of numerical simulations, all important processes have to be included in order to get simulation results that are close to reality. These shall be explained in the following. For further explanations, see Biellini [4], who implemented the physical properties into the applied research code MUFTE-UG.

### 2.1 Properties of CO<sub>2</sub>

Under atmospheric conditions, CO<sub>2</sub> is in a gaseous state. Besides, it can occur in different states of aggregation, depending mainly on temperature and pressure. In the case of geological CO<sub>2</sub> sequestration, these two parameters are influenced by the injection process and the depth where the injection takes place. Temperature and pressure in the subsurface are both increasing with depth. Higher pressure results in a higher CO<sub>2</sub> density, whereas higher temperatures decrease it. This can be seen in the phase diagram, figure 2.1.

In the case of carbon dioxide storage, the CO<sub>2</sub> can occur in a *liquid*, *gaseous* or in a *supercritical* state. Solid CO<sub>2</sub> is not discussed here because it does usually not occur under possible geological CO<sub>2</sub> storage conditions and is not of interest in this thesis. The *critical point* of CO<sub>2</sub> is at 304.19 Kelvin and 73.82 bar. If temperature and pressure exceed both values, the fluid is in a *supercritical state*. The temperature and the pressure are so high, that the density of liquid and gaseous CO<sub>2</sub> becomes equal and one single phase with continuous properties is obtained. This is depicted in figure 2.2. There, a gaseous and a liquid CO<sub>2</sub> phase are heated in a constant volume, until they exceed the critical point and form one phase.

Furthermore, when only temperature or pressure is varied, the fluid can switch the state of aggregation from supercritical to liquid or to gaseous without crossing the two-phase region of the saturation line, where a liquid and a gaseous CO<sub>2</sub> phase would

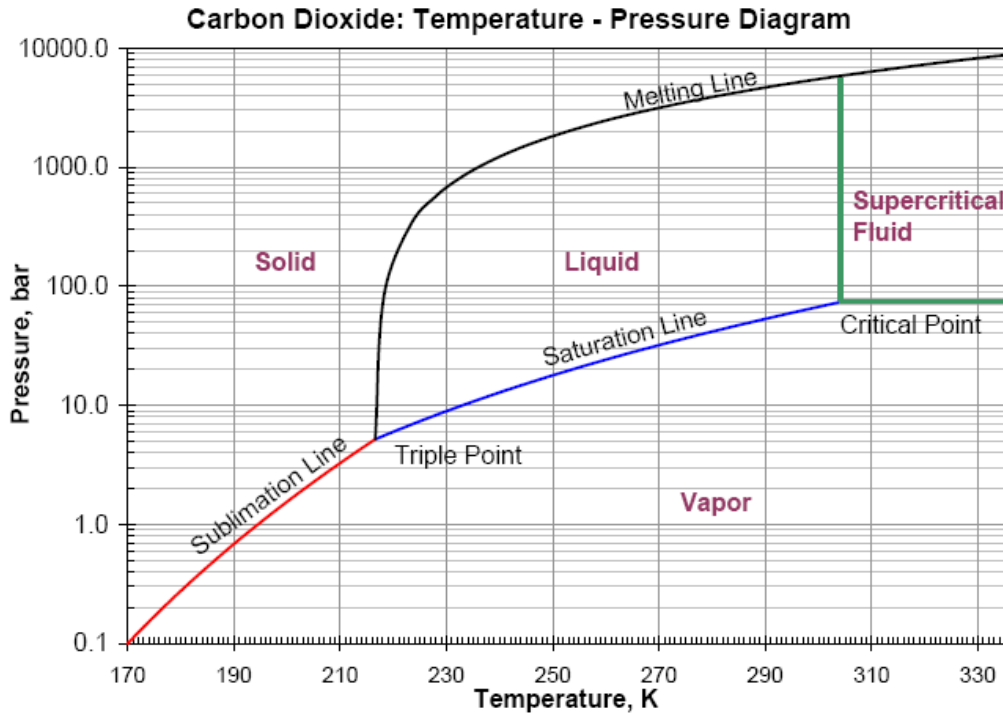


Figure 2.1: Phase diagram of CO<sub>2</sub>. It shows the different states of aggregation according to temperature and pressure. Created with CO<sub>2</sub>Tab, [www.chemicalogic.com](http://www.chemicalogic.com)

coexist.

Supercritical CO<sub>2</sub> is a good solvent for other substances such as methane and oil, which is adsorbed to soil particles or coal. In general, supercritical fluids have the advantage, that they have a high solubility and miscibility with other fluids, comparable to gases. The density and viscosity are more similar to a liquid substance. Thus, supercritical CO<sub>2</sub> can also be injected into depleted oil and gas reservoirs in order to increase recovery rates. This is already being applied in enhanced gas / oil recovery (EGR / EOR) and enhanced coal bed methane recovery (ECBM).

### 2.1.1 Density and Dynamic Viscosity

Density  $\rho$  describes the ratio of mass to volume of a substance. As can be seen in figure 2.3 (a), CO<sub>2</sub> density changes significantly with temperature and pressure. The density of CO<sub>2</sub> increases with incremental pressure whereas it decreases with incremental temperature. The range of occurring densities reaches from less than 10 to more than 700 kg/m<sup>3</sup>.

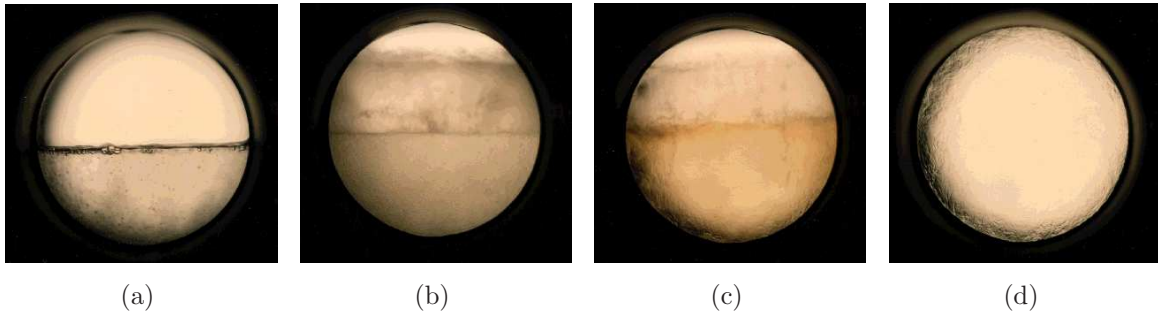


Figure 2.2: CO<sub>2</sub> switching from two phases (liquid and gaseous CO<sub>2</sub>) to the supercritical state due to an increase of temperature and pressure. The interface of the two phases is becoming more and more blurred, until one single phase is obtained. Source: [www.chem.leeds.ac.uk](http://www.chem.leeds.ac.uk)

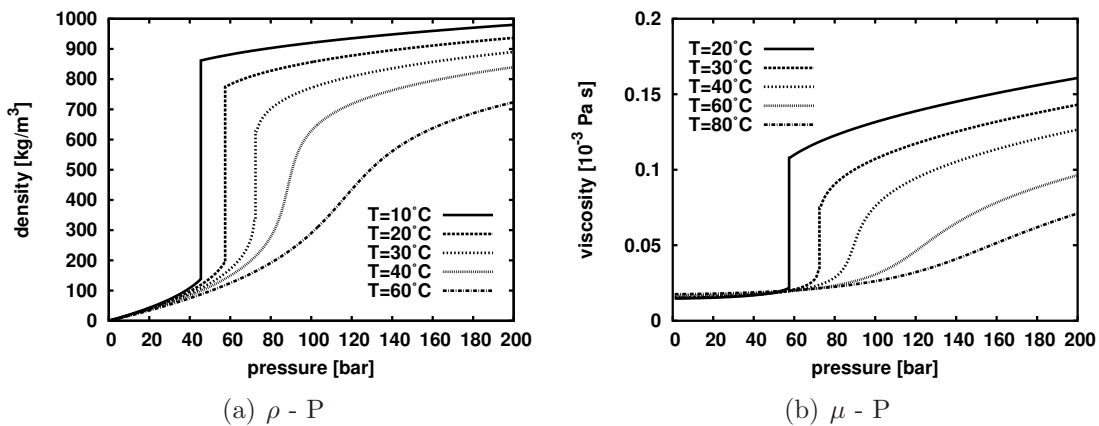


Figure 2.3: Density - pressure (a) and dynamic viscosity pressure diagram (b). Source: Bielineski [4]

Viscosity is a measure for the internal stickiness and resistance of a fluid against motion (shear stress). It describes the relation between the shear stress of a fluid to a velocity gradient:

$$\mu = \frac{\tau}{\partial v / \partial z}. \quad (2.1)$$

The viscosity of CO<sub>2</sub> has a similar developing with temperature and pressure as density. With increasing temperature, the fluid becomes more viscous. An increase of pressure has a decrease of viscosity as consequence. In figure 2.3 (b), this dependency is depicted. The range of occurring viscosities is from 1.4 E-5 Pa·s in shallow depths to more than 5 E-5 Pa·s in deep aquifers.

The biggest changes in the fluid properties occur, when the state of aggregation changes from gaseous to liquid or supercritical. This represents the fact, that gaseous CO<sub>2</sub> has less internal friction and a lower density than liquid or supercritical carbon dioxide. The two parameters temperature and pressure vary significantly with depth of the storage aquifer. The temperature gradient within different reservoirs can vary between 10 to more than 100 K/km. An average temperature gradient of 30 K per kilometer is common in storage sites and used throughout the thesis. This is also used for the determination of the CO<sub>2</sub> density and viscosity with depth. For this consideration, the pressure distribution in vertical direction is given by the sum of hydrostatic pressure and atmospheric pressure. The brine pressure can be calculated by using equation 2.2, which describes the hydrostatic pressure. The pressure gradient is roughly 1 bar per 10 meters depth (depending on brine density).

$$P_w = \rho_w \cdot g \cdot z + P_{atm} \quad (2.2)$$

With these two gradients it is possible to depict CO<sub>2</sub> viscosity and density as function of depth. Figure 2.4 shows this progress with increasing depth using the described temperature and pressure gradient.

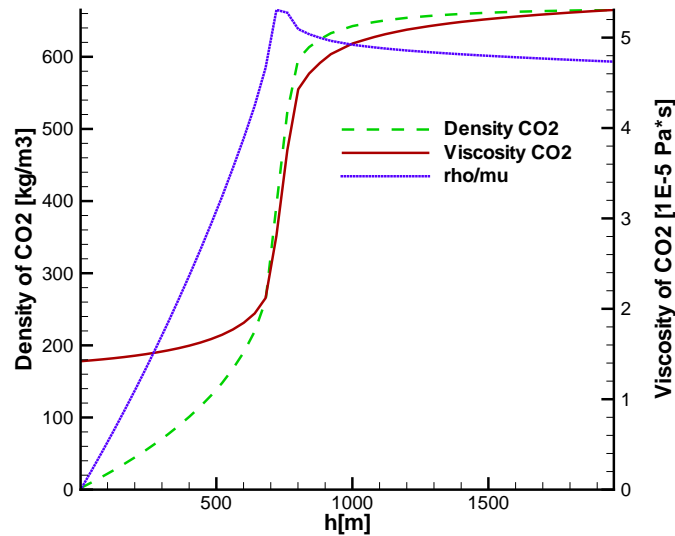


Figure 2.4: Density and dynamic viscosity of CO<sub>2</sub> over depth with a hydrostatic pressure distribution and a temperature gradient of 30 K/km. Moreover, the qualitative course of the ratio of density to viscosity is depicted.

One can see that the density in the upper 600 meters, where CO<sub>2</sub> is in a gaseous state, is low with less than 200 kg/m<sup>3</sup>. Then, the phase state changes from gaseous to supercritical and consequently the density increases remarkably, until it reaches values of over 600 kg/m<sup>3</sup> in depths of more than 800 meters. Depths of at least 700 meters

are to be favored for CO<sub>2</sub> storage, because the available pore space can be used best with the resulting high fluid densities. Another advantage is, that buoyancy forces are lower, because they depend on the density difference of CO<sub>2</sub> and brine.

### 2.1.2 Enthalpy

Enthalpy is a system property that describes the thermodynamic potential of a system. It is defined as sum of the internal energy that is stored in the substance and the volume-changing work that is applied on the system:

$$H = U + pV \quad (2.3)$$

For the determination of CO<sub>2</sub> enthalpies, the correlation by Span and Wagner [14] is used. The behavior with temperature and pressure is depicted in 2.5.

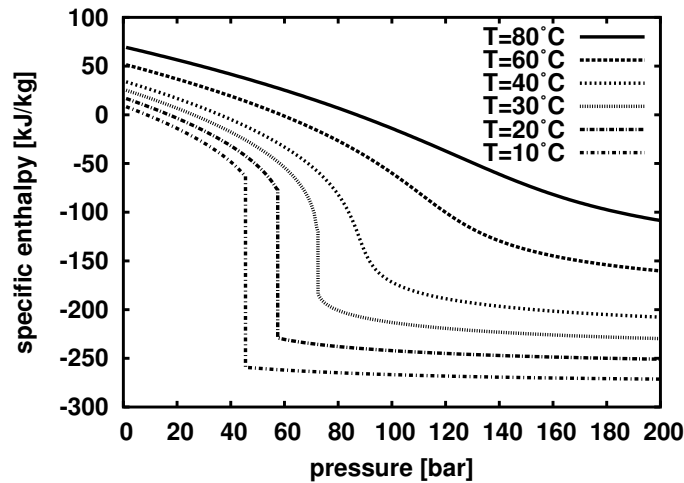


Figure 2.5: Development of the specific enthalpy of CO<sub>2</sub> with pressure and temperature. Source: Bielinski [4]

## 2.2 Properties of Brine

### 2.2.1 Density and Dynamic Viscosity

The mixture of water and salt, namely brine, has different properties than CO<sub>2</sub>. A higher pressure has the effect, that brine becomes denser, whereas a higher temperature causes an expansion of the fluid. With a constant temperature gradient of 30 K/km, density becomes less when getting into deeper zones. The temperature gradient has a stronger influence on the brine density than the increasing pressure, since compressibility of brine is very low. When other temperature gradients are

considered, this behavior may be different.

Furthermore, the effect of decreasing brine density with depth can be recognized, when a constant salt content in the brine is assumed. The density is affected if the salt content is changes with depth. A higher salt content increases brine density. Moreover, a higher salt content has effects on the dissolution behavior of carbon dioxide in brine. For the performed simulations, a constant salt content of the brine of ten mass percent was assumed. Consequently, brine density becomes lower with depth.

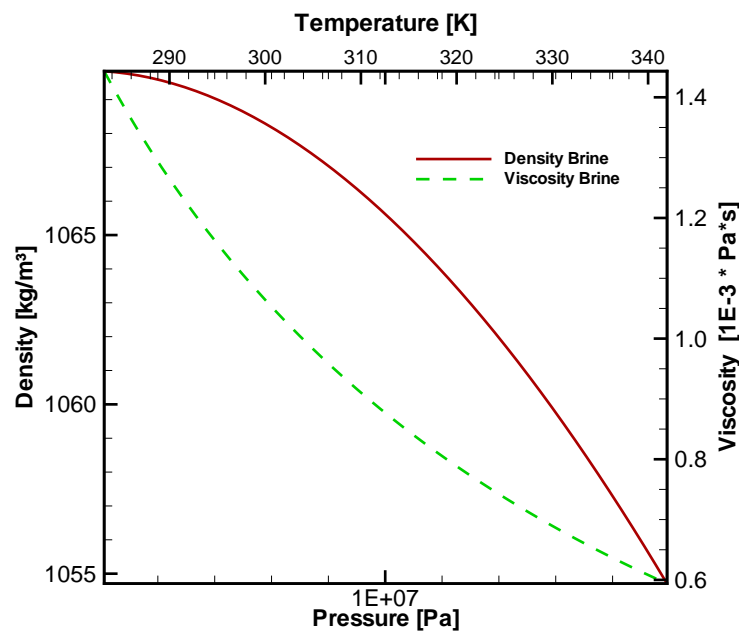


Figure 2.6: Density and dynamic viscosity of the formation brine with different pressures and temperatures.

The viscosity of brine has also a different behavior to that of  $\text{CO}_2$ . When temperature and pressure increase, brine viscosity is getting lower. With the used temperature gradient, it also decreases with depth. The development of density and viscosity with depth is depicted in figure 2.6. But the changes are small compared to the ones of carbon dioxide, since brine occurs only in a liquid state of aggregation, which does not change with depth.

### 2.2.2 Enthalpy

The brine enthalpy is depicted in figure 2.7. It increases with higher temperatures. Moreover, the salt content has an influence on the brine enthalpy.

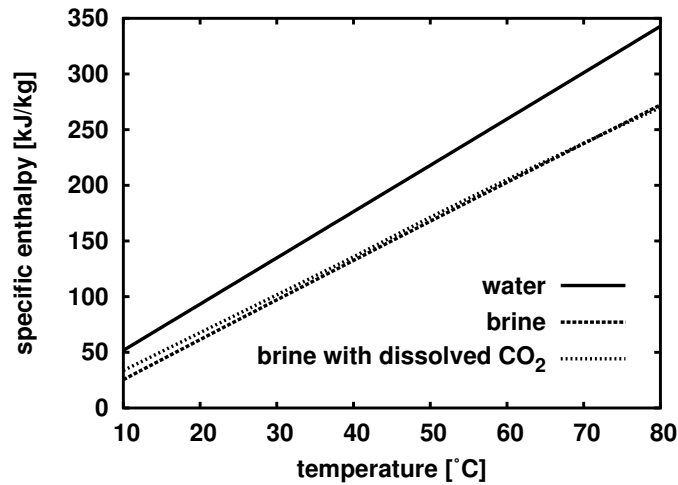


Figure 2.7: Development of the specific enthalpy of brine with pressure and temperature. Source: Bielinski[4]

## 2.3 Important Processes

To understand the behavior of carbon dioxide that is injected into the subsurface, one has to know the different processes that may occur. At the injection well, CO<sub>2</sub> enters the aquifer with a certain density difference to the brine depending on the pressure at the respective aquifer depth and the applied pressure at the injection. The forming plume will spread, mainly driven by pressure differences that are induced by the injection well. As it flows further away from the injection point, the influence of buoyancy, diffusion and advection driven by the formation water flow is increasing. Consequently, the CO<sub>2</sub> dissolves more and more in the formation brine. In a long-lasting process, the CO<sub>2</sub> may react with minerals of the formation rock. These different processes are explained in the following.

### 2.3.1 Solubility of the Fluids

The solubility of carbon dioxide is of special interest in the field of CO<sub>2</sub> sequestration, since it represents an important storage mechanism. When CO<sub>2</sub> is dissolved in the aqueous phase, it is taken with the background water flow into deeper regions. Solubility of CO<sub>2</sub> in brine is higher when salinity is lower. The dissolution of CO<sub>2</sub> in brine is taken into account by an attempt of Duan and Sun [6], who present a thermodynamic formula to calculate the maximum solvable CO<sub>2</sub> concentration. The behavior of the CO<sub>2</sub> solubility is depicted in figure 2.8. As can be seen, the solubility of CO<sub>2</sub> in brine becomes higher with higher pressures and lower with higher temperatures.

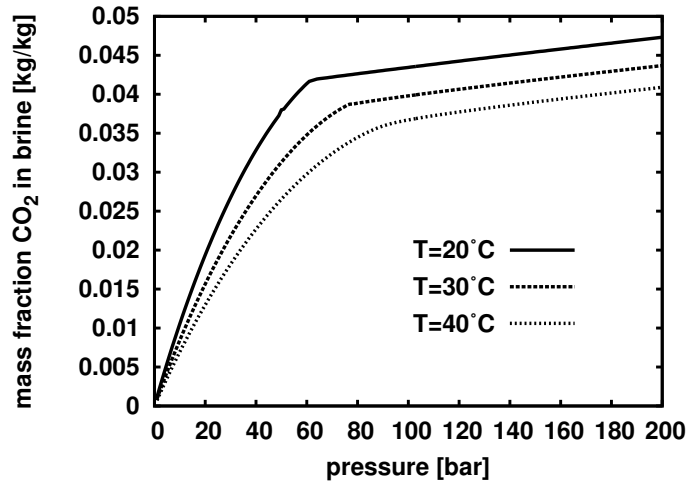


Figure 2.8: Solubility of CO<sub>2</sub> in the water phase in correlation to pressure, including several isotherms. Source: Bielineski [4]

### 2.3.2 Advection and Hydrodynamic Dispersion

Advection is the transport of a fluid due to a velocity field. Convection describes the same considering heat transport.

Molecular Diffusion is the movement due to concentration gradients and is caused by the motion of the molecules. It is a process that equalizes concentration differences. Dispersion is caused by fluctuations in a velocity field. For the models here, dispersion is not considered but diffusion is taken into account. Though, this process is of minor interest here, since CO<sub>2</sub> injection with the considered mass flows is dominated by advective and buoyancy forces. Diffusion is more important, when the long-term storage is examined.

### 2.3.3 Capillary Pressure

Capillary pressure at the pore scale describes the effect, that the pressures at the interface of two non-miscible fluids have a jump. The non-wetting phase (CO<sub>2</sub> phase) has a higher pressure than the wetting phase (the aqueous one). This difference is called capillary pressure and can be calculated on the micro scale using equation 2.4. It is proportional to the surface tension and to the contact angle, that the fluids describe at the interface. Smaller pores lead to higher capillary pressures.

$$P_c = \frac{4\sigma \cdot \cos(\alpha)}{d} \quad (2.4)$$

When the macro-scale is considered, the capillary pressure  $p_c$  is defined as the difference of the non-wetting and the wetting fluid. Through the averaging process from the micro-scale to the macro-scale, a non-linear relationship between capillary pressure

and phase saturation evolves. Different parameterizations exist, for example the ones from *Van-Genuchten* and from *Brooks and Corey*. The latter parameterization is used here. Following equations describe this parameterization:

$$p_c = p_D \cdot S_e^{-1/\lambda} \quad (2.5)$$

with

$$S_e = \frac{S_w - S_{w,r}}{1 - S_{w,r}} \quad (2.6)$$

For the capillary pressure - saturation relationship on the macro-scale, a Brooks-Corey function is applied with constant values for the residual saturation of the water phase  $S_{w,r}$  of 0.1 and for the CO<sub>2</sub> phase  $S_{CO_2,r}$  of 0.05. The entry pressure  $p_D$  is set to 22000 Pascal and the Brooks-Corey parameter  $\lambda$  equals 1.5. The chosen values for this curve are similar to data from Bachu et al. [3], which was measured in laboratory and field experiments in western Canada. He determined capillary pressure - saturation relationships for three kinds of sandstone and carbonate formations in sedimentary basins. The parameters determined for the sandstone reservoirs seem to be also suitable for the cases here, and are used in the models, since no better data was available. The curve that is applied has a similar entry pressure  $p_D$ , but a lower developing than the ones from Bachu.

### 2.3.4 Relative Permeability

This a rock-fluid property, that expresses the influence of the fluids on each other and the influence of the rock matrix on the flow behavior. Relative permeabilities have values between zero and one. Here, also a correlation between relative permeability and phase saturation exists. It can be described with different parametrizations. For the simulations, the formulation of Brooks and Corey was used, which has the form:

$$k_{r,w} = S_e^{\frac{2+3\lambda}{\lambda}} \quad (2.7)$$

$$k_{r,CO_2} = (1 - S_e)^2 \cdot (1 - S_e^{\frac{2+\lambda}{\lambda}}) \quad (2.8)$$

The same parameters as in the capillary pressure - saturation relationship were used. They are depicted in table 2.1:

### 2.3.5 Hysteresis

Hysteresis is not examined in this thesis here. But it should be clarified what this process is and what impact it might have. The effect is that relative permeability - saturation and the capillary pressure relationship have a different developing during a drainage (displacement of the wetting fluid by the non-wetting) than during an

Residual water saturation	$S_{w,r}$	0.10
Residual CO <sub>2</sub> saturation	$S_{CO_2,r}$	0.05
Brooks-Corey entry pressure	$p_D$	22000 Pa
Lambda	$\lambda$	1.5

Table 2.1: Brooks-Corey parameters for the capillary pressure - saturation and the relative permeability - saturation relationship.

imbibition (displacement of the non-wetting water phase by the wetting CO<sub>2</sub> phase). The residual saturation is then not a fixed value but is changing, depending on the ongoing process and the history of the system. Moreover, the relation of the capillary pressure and the relative permeability to the saturation is not unique.

Hysteresis has mainly a positive effect on long-term storage of CO<sub>2</sub>. Hysteresis usually occurs in a homogeneous medium, when CO<sub>2</sub> is already injected and the well is turned off. It leads to more CO<sub>2</sub>, that is residually trapped in the pores, since the effect of hysteresis is that the residual CO<sub>2</sub> saturation is changed to a higher value. This leads to the description on different criteria and trapping mechanisms, that are important for long-term storage of carbon dioxide.

## 2.4 Criteria for Storage Reservoirs and Trapping Mechanisms

### 2.4.1 Trapping Mechanisms

In order to understand CO<sub>2</sub> storage in saline aquifers, the different mechanisms, that prevent the CO<sub>2</sub> from escaping the storage site and that increase storage security should be known. They are listed and explained in the following.

– **Stratigraphic and structural trapping**

Usually, CO<sub>2</sub> is injected into an aquifer which is situated under a geologic formation with a lower permeability. This uses the mechanism, that the low permeable layer forms a barrier for the CO<sub>2</sub> plume and prevents it from moving upwards e.g. due to buoyancy forces. This low permeable layer is called cap rock, and has ideally an intrinsic permeability, which is several orders lower than the permeability of the storage aquifer. For secure storage, different structures like domes or certain faults are beneficial. The injected plume migrates upwards and becomes trapped there.

– **Residual trapping**

The residual saturation describes a part of a fluid in the pores of a volume which is not drainable by advective forces. Residual trapping occurs when the saturation drops, e.g. due to dissolution processes or buoyancy effects. The saturation usually does not drop to zero. A certain part is kept back in small pores, which cannot move anymore and is trapped there by capillary forces. Moreover, the effect of hysteresis positively influences the amount of CO<sub>2</sub>, that is residually trapped.

– **Hydrodynamic trapping**

This is a trapping mechanism, which is the result of a moving water flow system. Without the flow, the injected carbon dioxide would move upwards and escape the aquifer. But the flow forces the CO<sub>2</sub> to flow into deeper regions or to stay where it is. This is a trapping mechanism, that is of interest in this thesis, since the ambient water flow in down dip direction poses the possibility to use this mechanism.

– **Solubility trapping**

Carbone dioxide, that is injected into a saline aquifer, dissolves to a certain amount in the aquifer brine. This is an ongoing process which takes relatively long and is influenced by temperature and pressure and the salt content of the brine. The brine density is increasing, when CO<sub>2</sub> is dissolved. This enforces a downwards movement of the brine with the higher density and increases storage safety. Moreover, since it is not a separate phase anymore, there are no buoyancy effects acting, that drive the CO<sub>2</sub> upwards.

– **Mineral trapping**

This is a process, that takes very long. It describes the effect, that CO<sub>2</sub> reacts with soil minerals and is then securely stored as chemical compound. This mechanism is not taken into account in this thesis, since the considered time scale is so short that this process has a negligible influence.

Potential target reservoirs should meet several criteria in order to provide a high storage security and enable an economic sequestration. A *confining layer* on top the storage aquifer, which has a considerable lower permeability (at least several orders of magnitude) is usually required. It has to prevent the CO<sub>2</sub> from rising upwards and to form a geological barrier for the gas. Moreover, the potential storage aquifer should have a *depth* of more than 700 meters, so that the injected CO<sub>2</sub> is in a liquid or even supercritical state. Enough *storage space* is required. Therefor the aquifer porosity should be high. Moreover, it should be possible to reach high injection rates into the reservoir with a technically feasible injection pressure. Therefor, the *permeability* of the storage reservoir should be high enough.

# Chapter 3

## Model Concept

### 3.1 Fundamental Terms

In order to get clarity about the terms that are used in this thesis, several definitions and explanations are made.

#### 3.1.1 Phases and Components

##### 3.1.1.1 Phases and Their State

*Phases* ( $\alpha$ ) are defined as homogeneous chemical substance or mixture of components with a distinct boundary to other phases. Each phase has its own chemical composition and physical properties, which may change abruptly at the interface between the phases. An illustrative example is oil and water: they can be considered as different phases. If oil and water are put into a vessel, they do not mix up with each other but form two different phases with a distinct interface to each other.

In the case of CO<sub>2</sub> sequestration into fully water-saturated saline aquifers, two fluid phases can be considered: One CO<sub>2</sub>-rich phase (described by the subscript CO<sub>2</sub> or n) and a water-rich phase (subscript w). Moreover, a solid phase is present in the form of soil or rock matrix. This phase is of minor interest here, because within the simulations it is assumed that it does not take part in any reactions, transitions or shrinking processes. It is assumed to be rigid.

Fluid phases can also be classified considering their wetting character. Here, water is the wetting fluid, whereas CO<sub>2</sub> is the non-wetting part of the two.

##### 3.1.1.2 Components

The term *component* ( $\kappa$ ) refers to the constituents of a phase. The components form the chemical composition of the phases. In the performed simulations, two components are considered, namely brine and CO<sub>2</sub>.

### 3.1.2 Representative Elementary Volume, REV

In numerical simulations, usually not each single pore is considered. This means, not all micro scale effects are taken into account separately but averaged over certain sub volumes, so-called *representative elementary volumes* (REV). This leads to a macro-scale consideration of flow- and transport processes. The REV size should be at least that big, that the properties can be considered as homogeneously distributed within one REV and small scale effects like fluctuations of the porosity are averaged out. Through this averaging process, new parameters like porosity and saturation evolve. Furthermore, new constitutive relationships like the capillary pressure - saturation relationship and the relative permeability - saturation relationship are introduced. They are described and explained below.

#### 3.1.2.1 Porosity

The free pore volume that can be occupied by fluids in a certain volume of a porous medium is called porosity. It is kept constant in the simulations and can be calculated in the following way:

$$\Phi = \frac{V_w + V_n}{V_{total}} \quad (3.1)$$

#### 3.1.2.2 Saturation and Mass Fraction

The volume of the free pore space in a REV, that is occupied by one phase, is called *saturation* of the phase. The saturations of all phases add up to one:

$$S_\alpha = \frac{V_\alpha}{\sum_\alpha V_\alpha} \quad (3.2)$$

$$\sum_\alpha S_\alpha = 1 \quad (3.3)$$

The superscript  $\kappa$  is used for the components and the subscript  $\alpha$  refers to the phases. The term *mass fraction* relates to the composition of the phases. It describes the share of a component within a phase. Mass fraction are determined as shown in equation 3.4. Again, the sum of all mass fractions within one phase add up to one (see equation 3.5). Another way to describe the composition of the phases is with the help of mole fractions. For this thesis, mass fractions are used.

$$X_\alpha^\kappa = \frac{m_\alpha^\kappa}{\sum_\kappa m_\alpha^\kappa} \quad (3.4)$$

$$\sum_\kappa X_\alpha^\kappa = 1 \quad (3.5)$$

## 3.2 Conceptual Model

For the simulations, a non-isothermal model concept including two phases with two components is used. This was developed by Class et al. [5] The water phase implemented in the model has the components water, dissolved CO<sub>2</sub> and salt. The salt component is not varied here but assumed to be constant. The CO<sub>2</sub> phase contains the components CO<sub>2</sub> and dissolved water. The components can be transferred from one phase to another through processes like evaporation, condensation, diffusion, solution and degassing processes or chemical reactions. This is schematically shown in figure 3.1. Therefore, thermal effects have to be taken into account and a non-isothermal model concept is used.

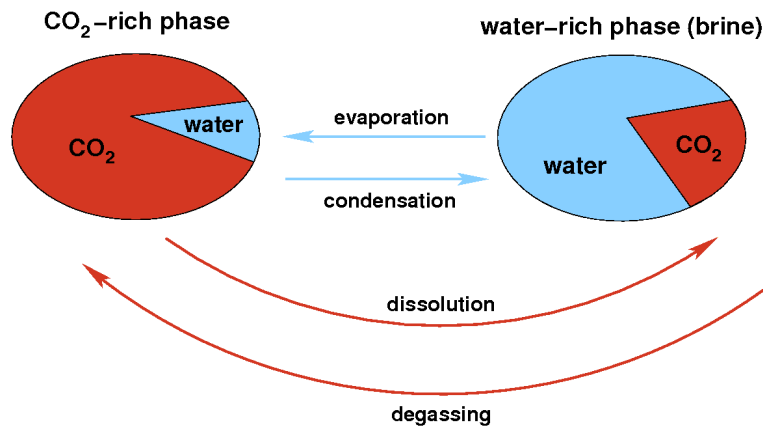


Figure 3.1: The used model concept considers two phases, two components and non-isothermal processes like evaporation and condensation.

## 3.3 Mathematical and Numerical Model

Different balance equations need to be taken into account for the formulation of the mathematical model. These comprise an energy equation and a momentum equation for each phase. These equations can be derived using the Reynold's transport theorem, as shown e.g. in Helmig [7] and shall be shown in the following. Moreover, the mass balance equation has to be fulfilled. The velocities are calculated using the extended version of the Darcy's Law for multiple phases:

$$v_{\alpha} = -\frac{k_{r\alpha}}{\mu_{\alpha}} \cdot \mathbf{K} \cdot (\nabla p_{\alpha} - \rho_{\alpha} \cdot \mathbf{g}); \quad (3.6)$$

### 3.3.1 Governing Equations

The physical flow processes can be described by a set of coupled partial differential equations. They are of hyperbolic/parabolic type and are highly non-linear. For the

description of the mass balances, each phase has to be considered separately. The balance equation for each phase is depicted in equation 3.7. Moreover, a constant porosity distribution over the entire domain is assumed.

$$\begin{aligned}
& \underbrace{\phi \frac{\partial (\sum_{\alpha} \rho_{\alpha} X_{\alpha}^{\kappa} S_{\alpha})}{\partial t}}_{\text{storage term}} \\
& - \underbrace{\sum_{\alpha} \nabla \cdot \left\{ \frac{k_{r\alpha}}{\mu_{\alpha}} \rho_{\alpha} X_{\alpha}^{\kappa} \mathbf{K} (\nabla p_{\alpha} - \rho_{\alpha} \mathbf{g}) \right\}}_{\text{advective transport}} \\
& - \underbrace{\nabla \cdot \{ D_{pm}^{\kappa} \rho_w \nabla X_w^{\kappa} \}}_{\text{diffusive transport}} \\
& - \underbrace{q^{\kappa}}_{\text{sources/sinks}} = 0 \quad \kappa \in \{w, CO_2\}, \alpha \in \{w, CO_2\} \quad (3.7)
\end{aligned}$$

As can be seen in the mass balance equation, it consists of four different parts:

- the storage term accounts for mass storage
- the advective transport term describes flow initiated by pressure and density differences
- diffusive transport due to concentration gradients is taken into account by the third term
- the last term describes sources and sinks

For the energy balance, local thermal equilibrium is assumed. That means that all phases and the rock matrix at one point have the same temperature. This assumption can be made, because heat exchange between the phases happens very fast in comparison to other processes like advection or diffusion. Consequently, only one energy balance needs to be solved for the system:

$$\begin{aligned}
& \underbrace{\phi \frac{\partial (\sum_{\alpha} \rho_{\alpha} u_{\alpha} S_{\alpha})}{\partial t} + (1 - \phi) \frac{\partial (\rho_s c_s T)}{\partial t}}_{\text{storage term}} - \underbrace{\nabla \cdot (\lambda_{pm} \nabla T)}_{\text{heat conduction}} \\
& - \underbrace{\sum_{\alpha} \nabla \cdot \left\{ \frac{k_{r\alpha}}{\mu_{\alpha}} \rho_{\alpha} h_{\alpha} \mathbf{K} (\nabla p_{\alpha} - \rho_{\alpha} \mathbf{g}) \right\}}_{\text{convective transport}} \\
& - \underbrace{q^h}_{\text{sources/sinks}} = 0 \quad \alpha \in \{w, CO_2\} \quad (3.8)
\end{aligned}$$

There are again different terms in equation 3.8 which are similar to the ones in the mass balance equation 3.7. It consists also of a storage term, heat transport due to convection and a source and sink term. Additionally, a term that describes heat conduction occurs.

### 3.3.2 Discretization Scheme

For modeling purposes, the numerical simulator MUFTE-UG [8] was used, which is a modular research code. It is adaptable to different problem structures and includes several solution methods and discretization schemes. The physical properties and processes can be implemented directly into the code, which is written in the computer language C.

The used time discretization scheme uses a fully implicit Euler time discretization, which is unconditionally stable. For the spatial discretization, different methods exist. The ones that were used for the simulation were

- the Box method
- the controlled volume finite element method (CVFE)

The 2D-simulations were performed using the Box method, which is a mass-conservative Subdomain Collocation Method. A detailed description of the box scheme can e.g. be found in Class [5] or in Huber [10]. A controlled volume finite element (CVFE) discretization scheme is applied for the spatial discretization of the 3D-simulations. It is also strictly mass-conservative. The CVFE was chosen for 3D, because it takes also diagonal fluxes into account and thus produces more realistic simulation results in the case of an advective dominated model. In two-dimensional space, it uses a 9-point approximation to calculate the fluxes within one volume, whereas the Box scheme uses a 5-point approximation.

The reason for this is a different calculation of the fluxes: The Box method calculates fluxes over the different volume faces of the sub control volumes. That means, it takes fluxes over a subcontrol volume face from the neighboring four cells (2D) into account. The CVFE calculates fluxes by volume integrals of the masses in sub volumes of all eight surrounding cells. The CVFE discretization method is explained further in Huber [10].

### 3.3.3 Primary and Secondary Variables

For modeling purposes, suitable primary and secondary variables have to be chosen. Primary variables are calculated directly within the iteration steps of the numerical model, whereas the secondary variables are calculated from the primary ones. Applying the Gibbs'ian phase law 3.9 for the macroscopic consideration to the problem structure (two phases  $\alpha$ , two components  $\kappa$ , non-isothermal) shows that three

independent primary variables for the degrees of freedom (F) have to be chosen in order to get a unique solution:

$$F = \kappa + 1 \quad (3.9)$$

As the first two primary variables, the pressure of the CO<sub>2</sub>-phase ( $p_n$ ) and the system temperature (T) are chosen. The temperature is assumed to be equal in all phases at each point within the domain, as mentioned before.

The third primary variable is a special one, which does not always describe the same parameter but can switch its definition. This is described further in Class [5]. Depending on different criteria, it is either defined as water saturation  $S_w$ , mass fraction of CO<sub>2</sub> dissolved in the water phase  $X_{CO_2,w}$  or mass fraction of water in the gas phase,  $X_{w,g}$ .

This is decided according to the phase state along with different switch criteria (summarized in table 3.1):

- When there is only a water phase present ( $S_w = 1$ ), where the maximum amount of dissolved CO<sub>2</sub> has not been reached (switch criterion), the variable represents the mass fraction of CO<sub>2</sub> dissolved in the water phase.
- In the case of both phases present ( $0 < S_w < 1$ ), when the mass fraction of CO<sub>2</sub> or the one of water exceeds the maximum solvable concentration, the variable contains the saturation of the wetting phase,  $S_w$ .
- And, if there is no water phase present ( $S_w = 0$ ) but only a gas phase, it shows the mass fraction  $X_{w,g}$  of water within the gas phase. The state changes, when the maximum solvable amount of water within the gas phase is reached

Present phases	Criteria	Variable type	Switch Criteria
Water phase	$S_w = 1$	$X_w^{CO_2}$	$X_w^{CO_2} > X_{w,max}^{CO_2}$
Both phases	$0 < S_w < 1$	$S_w$	$S_w < 0$ or $S_n < 0$
Gas phase	$S_w = 0$	$X_n^w$	$X_n^w > X_{n,max}^w$

Table 3.1: Adaptive choice of primary variables

The secondary variables are derived from the primary variables. The most important secondary variables are water pressure  $p_w$ , CO<sub>2</sub> saturation  $S_n$ , mass fractions, viscosities and densities.

The water pressure and the CO<sub>2</sub> saturation can be calculated from the primary variables using the following constitutive relationships:

The pressure of the water phase equals the difference of the pressure of the CO<sub>2</sub> phase and the capillary pressure:

$$p_w = p_n - p_c \quad (3.10)$$

The saturation of the water phase is the difference of the saturation of the CO<sub>2</sub> phase to one:

$$S_n = 1 - S_w \quad (3.11)$$

For the other secondary variables, the constitutive relationships that are shown in the chapter Physical Properties are used.

The mass balance and the energy balance equation are linearized using an inexact Newton-Raphson technique. The linearized Jacobian system is solved with a stabilized Bi-Conjugated Gradient method (Bi-CGStab). With the inexact linearization of the partial differential equation, a defect is made which is iteratively minimized with the weighted-residuals method. The advective part of the equations is computed using a fully-upwinding technique. For further details, see e.g. Bielinski [4] or Helmig [7].

# Chapter 4

## 2D Simulations

### 4.1 General Setup

Figure 4.1 shows the setup that was chosen for the two-dimensional models. A rectangular model area is counterclockwise rotated around the lower left corner with a dip angle  $\alpha$ . It has a length of 1500 meters and a height of 40 meters. The geometry is kept constant for the simulations. The models include an ambient formation water flow from the higher situated east boundary to the lower west boundary. The injection well with a constant pressure is situated in the middle of the reservoir. The bottom of reservoir (BOR) was adapted, when the dip angle is changed, so that the depth of the injection well (DOI) is situated at a well-defined level. The model axes are oriented with the aquifer geometry. The Z-axis is perpendicular to the aquifer top and the X-axis is parallel to it.

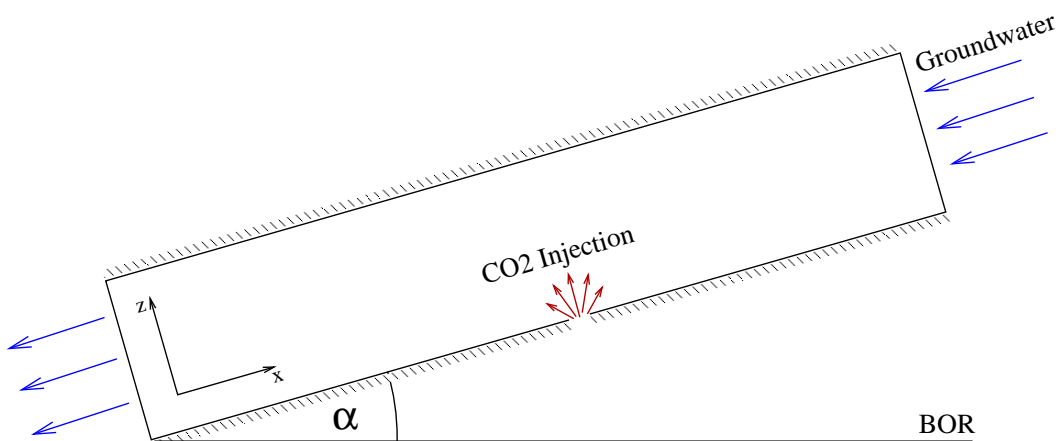


Figure 4.1: Simulation setup

For the simulations, following assumptions were made:

- the parameter distribution within the reservoir is homogeneous
- no heterogeneities are included
- the porous medium is rigid and does not take part in any reactions
- an impermeable layer is on top of the storage reservoir
- friction between the water phase and the CO<sub>2</sub> phase are not taken into account

#### 4.1.1 Description of the Used Mesh

The mesh that was used here is coarse at the side boundaries and becoming finer in the vicinity of the well. It consists of  $100 \cdot 16 = 1600$  nodes with rectangular elements.

## 4.2 Initial Values and Boundary Conditions

The *initial values* of the simulation were set as hydrostatic pressure distribution plus the pressure that is applied by the formation water flow on the system. At the beginning of the simulation, the aquifer is set as fully water-saturated without any CO<sub>2</sub> phase. The temperature distribution is described by a geothermal gradient of 30 K/km. At the surface, a temperature of 283.15 K is assumed.

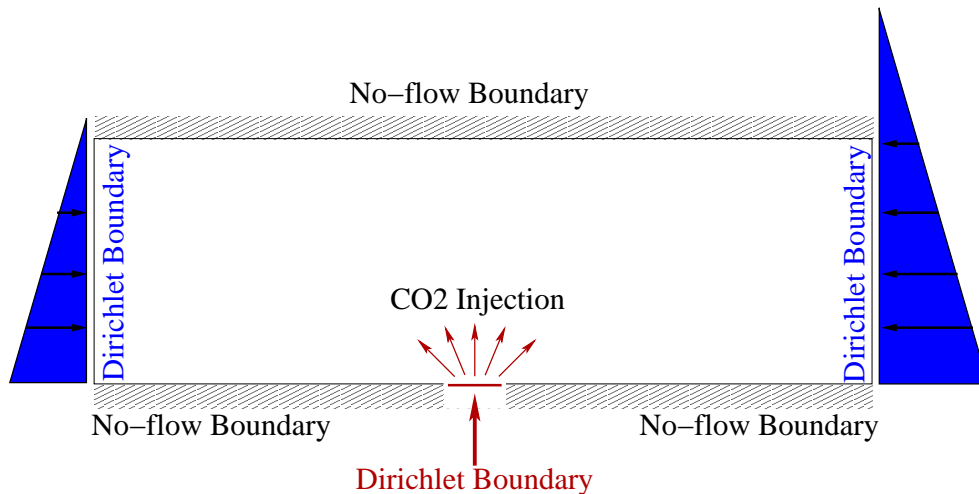


Figure 4.2: 2D boundary conditions

In figure 4.2, the setup of the *model boundaries* is depicted. The west boundary was set to values that represent hydrostatic pressure conditions by using a Dirichlet boundary condition. At the opposite boundary in the east, a water flow was introduced by adding pressure to the hydrostatic pressure. This additional pressure is referred to as flow pressure  $P_{flow}$  in the following. A Dirichlet boundary was chosen here, too,

because a Neumann-boundary would hinder the CO<sub>2</sub> from flowing upwards, especially when it gets close to the boundary. This would influence the propagation behavior of the CO<sub>2</sub> phase more than the Dirichlet boundary. With the two Dirichlet boundaries it is possible to examine the flow direction of the injected plume and to take also effects from the injection on the water flow into account.

The north boundary is defined as no-flow boundary. It was set as impermeable barrier for both phases, CO<sub>2</sub> and water. This is a simplification, that was made here, because it is assumed, that the confining cap rock has a permeability, which is several orders of magnitude lower than in the storage aquifer. Moreover, the entry behavior of the CO<sub>2</sub> phase into the cap rock shall not be discussed here.

The major part of the south boundary is set as no-flow boundary, too. A small part with a length of 15 meters in the middle of the south boundary is left open for injection by using a Dirichlet boundary. Here, the pressure is defined as the pressure that is in the aquifer before the injection starts plus an additional injection pressure,  $P_{inj}$ . When this injection pressure equals zero, the CO<sub>2</sub> flow into the model domain is also zero. A Dirichlet boundary was applied here, in order to have a well defined pressure in the middle of the reservoir. A Neumann boundary would create a varying pressure field with fluctuations in the numerical simulation. With that, it would be difficult to get an impression of the behavior.

The pressures at the two side boundaries and the injection over a small area in the middle of the south boundary are implemented in the following way:

- Water pressure at the west boundary:

$$P_{w,west} = \sin(\alpha) \cdot \rho_{w,1} \cdot g \cdot h_{west} + P_{atm} - P_d \quad (4.1)$$

- Water pressure at east boundary:

$$P_{w,east} = \sin(\alpha) \cdot \rho_{w,2} \cdot g \cdot h_{east} + P_{atm} - P_d + P_{flow} \quad (4.2)$$

Since  $P_n$  and  $S_w$  are chosen as primary variables, the capillary pressure  $P_d$  has to be deduced at the Dirichlet side boundaries (see equation 3.10) in order to define the water pressure properly. Moreover, the dip angle of the aquifer has to be taken into account when defining the hydrostatics.

- Injection pressure for the CO<sub>2</sub> phase at south boundary:

$$P_{w,inj} = \sin(\alpha) \cdot \rho_{w,3} \cdot g \cdot h_{inj} + P_{atm} + 0.5 \cdot P_{flow} + P_{inj} \quad (4.3)$$

Brine density  $\rho_w$  changes with aquifer depth as shown before. The dip angle leads to different depths at the boundaries. Hence, the densities used at the east, west and

south boundary were adjusted with respect to the governing pressure and temperature at each border. Same applies for the injection temperature of the CO<sub>2</sub> phase. It was chosen in a way, that it has the same temperature as the brine at the place of injection.

### 4.3 Description of the Reference Model

A reference model is created including formation water flow and a dip angle of 4°. The dip angle was chosen according to the median value of an American oil reservoir database, which is described below. The reference case is used to compare different parameter setups and their influence on the propagation behavior and to explain different occurring processes. Parameters, that were not varied but kept constant in the different cases can be found in table 4.1:

Geothermal gradient [K/km]	30
Porosity [-]	0.2
Aquifer Length [m]	1500
Aquifer Height [m]	40
Salt content [Mass-%]	10
Anisotropy [-]	0.1

Table 4.1: Constant parameters of the 2D simulations

The injection pressure ( $P_{inj}$ ) was set to 4E5 Pascal over aquifer pressure, which is below cap rock fracture pressure and roughly in the range of injection pressures that are applied for CO<sub>2</sub> storage. However, the injection pressure in two-dimensional simulations cannot be transferred directly to three-dimensional space. The injection pressure of 4E5 Pascal results in an average injection rate of 0.036 kg/(s·m) in the reference case. Note that this is the mass flow per meter width of the aquifer, since this is a two-dimensional analysis.

After determining an injection pressure, the pressure for the brine flow ( $P_{flow}$ ) at the east boundary was set. With 8E5 Pascal additional pressure at the east boundary, the major part of the injected CO<sub>2</sub> moves downwards. The average formation water flow velocity amounts then to 6E-7 m/s. This is in the range of natural flow velocities in the subsurface.

These values were used for the injection and the water flow pressure in the reference case. Then, parameters with a strong influence on the fluid flow pattern were identified and varied. The parameters that were examined further are the dip angle and depth of the aquifer, the injection pressure at the well, the flow velocity of the formation

brine, anisotropy and permeability of the aquifer. The parameters that were varied were chosen for the reference case, as shown in table 4.2.

Dip angle [°]	4
Injection depth [m]	1000
$\Delta P_{inj}$ [Pa]	4E5
$\Delta P_{gw}$ [Pa]	8E5
Hor. permeability [m <sup>2</sup> ]	1E-12

Table 4.2: Parameters used for the reference case

The values were selected, because they are all within the range of a public reservoir database created by the U.S National Petroleum Council (NPC) in 1984. This is further analyzed in the research proposal by Kopp [11], where the occurring parameter bandwidths are examined and summarized. Since no comparable database for deep saline aquifers exists, the bandwidths which were listed there are used to delimit the parameter bandwidth for the considerations here. The examined bandwidths lie well within the range of the database. It is assumed that the parameters of saline reservoirs are not very different to the ones of the NPC reservoir database and that these parameters are representative for real storage sites. For the reference case, mainly the rough average values of the database were used.

Three exemplary saturation profiles of the reference case are shown in figure 4.3. These reveal, that the shape of the resulting plume is highly complex and that it is influenced by various non-linear processes and parameters.

## 4.4 Determination of the Flow Direction

An essential question of storing CO<sub>2</sub> into a dipped aquifer with a background water flow is, in which direction the evolving plume propagates. To determine the predominant flow direction of the plume, the forces that are governing the system have to be identified and somehow quantified. During the injection, these are mainly buoyancy and viscous forces. The influence of capillary forces is of minor interest here, since the pressures that arise from the injection and the water flow are assumed to have a stronger influence on the fluid flow pattern at the field scale during the injection. The viscous forces originate on the one hand from the injection and on the other hand from the water flow, which are both represented by additional pressures at the boundaries within the simulations. Buoyancy forces have their origins in density differences of the two fluid phases and are very strong, when the CO<sub>2</sub> phase has a low density.

It is of interest, whether the injected plume rises up dip or down dip. In order to determine this, the pressure gradient in X-direction has to be considered. First, a dipped

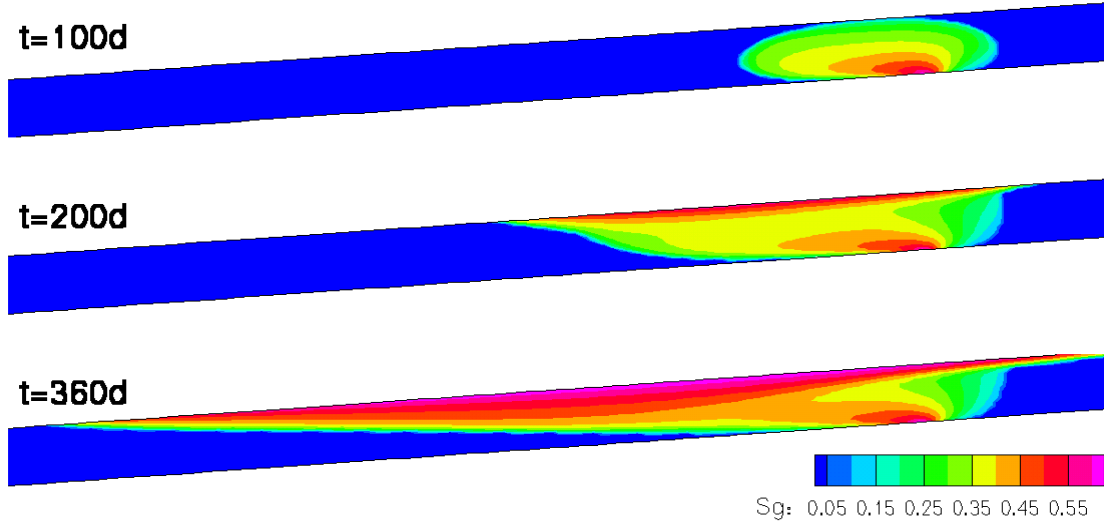


Figure 4.3: Saturation profile of the reference case at three different points in time. The images show the propagation behavior at a section from  $X=100\text{m}$  to  $X=900\text{m}$  with the injection well at  $X=750\text{m}$ .

aquifer without injection is regarded. The pressure gradient in positive  $X$ -direction comprises the pressure gradient due to the formation water flow. Furthermore, the hydrostatic pressure gradient has to be taken into account. Equations 4.4 and 4.5 describe the pressure gradients that are relevant for this problem, further. For this consideration, brine density is assumed to be constant.

Furthermore, the pressure gradient that leads to the formation water flow ( $\nabla P_{flow,x}$ ) has to be determined. In the simulations, this is the additional water pressure to the hydrostatic pressure at the east boundary ( $P_{flow}$ ) divided by the length of the aquifer, as described in equation 4.4. This gradient is defined negative, since it acts in the negative  $X$ -direction.

$$\nabla P_{flow,x} = -\frac{P_{flow}}{LengthX} \quad (4.4)$$

Due to the dip of the aquifer, the  $X$ -component of the gravity vector also contributes to the arising pressure distribution parallel to the aquifer bottom. It takes effect in the positive  $X$ -direction and is pointing in up dip direction. The pressure gradient due to gravity forces and dip angle of the aquifer is constant throughout the aquifer, since a constant dip angle and brine density is assumed. It is calculated as the sinus of the dip angle times the hydrostatic pressure gradient, as shown in equation 4.5:

$$\nabla P_{grav,x} = \sin(\alpha) \cdot g \cdot \rho_w \quad (4.5)$$

The resulting pressure gradient in X-direction is obtained by the sum of equations 4.4 and 4.5:

$$\begin{aligned}\frac{\partial p_\alpha}{\partial x} &= \nabla P_{grav,x} + \nabla P_{flow,x} \\ &= \sin(\alpha) \cdot g \cdot \rho_w - \frac{P_{flow}}{LengthX}\end{aligned}\quad (4.6)$$

The pressure field due to the groundwater flow and dip angle without injection has a linear development, from one side boundary of the aquifer to the other one. A horizontal pressure field would indicate that no water flow takes place due to viscous forces.

When the injection starts, the injection pressure evolves ( $P_{inj}$ ). The linear pressure field of the groundwater flow is superimposed by an elliptical injection pressure field. It shows up to be a crucial parameter for the propagation behavior. At the injection well, a constant injection pressure is applied which describes the difference of the pressure when the injection is turned on to the undisturbed aquifer pressure including the groundwater flow.

The pressure distribution in the aquifer is not constant but changes over time. The injection pressure gradient in X-direction cannot be calculated exactly, since it has a complex shape. But for the estimation of the flow direction, it can be assumed to equally release in both directions, up dip and down dip. Furthermore, it is assumed, that the pressure at the cap rock directly above the injection is also increased by the injection pressure. The performed simulation runs were in good agreement with these assumptions. This leads to a well-defined pressure in the vicinity of the well and hence an approximate pressure gradient of the injection can be determined.

The applied injection pressure can then be expressed as pressure gradient by dividing it by the distance from the injection to the upper water inflow boundary. With this, a linear development of the aquifer pressure is assumed. This approximation leads to the fact, that the injection gradient is rather overestimated in the positive X-direction. In reality, the pressure would release faster. Since the pressure development of the injection is of elliptic shape which is difficult to describe, a linear approximation is used for this gradient. It is shown in equation 4.7.

$$\nabla P_{inj,x} = \frac{P_{inj}/2}{\Delta X} = \frac{P_{inj}}{LengthX}\quad (4.7)$$

This can be justified, because the vertical height of the aquifer is much lower than the horizontal extent. Moreover, the vertical permeability is also less than the horizontal one due the influence of the anisotropy of the intrinsic permeability.

The difference of the two pressures gradients has a strong influence on the arising pressure field and subsequently on the movement of the plume. The injection pressure

works against the groundwater flow in the aquifer part upstream the injection well and with the groundwater flow in the downstream part. When the aquifer is dipped, the influence of buoyancy, which was determined before, has to be taken into account as well. The resulting pressure gradient in the X-direction from the well up to the east inflow boundary sums up to

$$\begin{aligned} \frac{\partial p_\alpha}{\partial x} &= \nabla P_{flow,x} + \nabla P_{grav,x} + \nabla P_{inj,x} \\ &= -\frac{P_{flow}}{LengthX} + \sin(\alpha) \cdot g \cdot \rho_w + \frac{P_{inj/2}}{\Delta X}. \end{aligned} \quad (4.8)$$

Note that the groundwater pressure gradient has a negative value, whereas the other gradients are positive. With the above mentioned simplifications, the arising pressure distribution between the injection well and the east boundary with the groundwater inflow can be described as linear. The acting pressure forces are schematically depicted in figure 4.4.

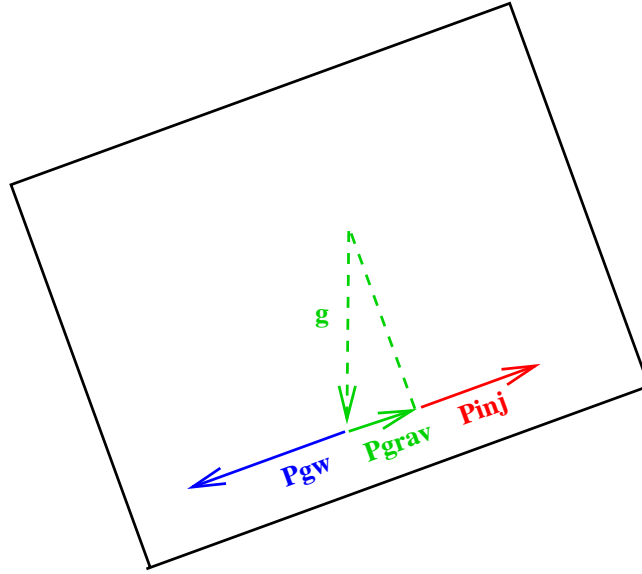


Figure 4.4: The different pressures gradients that act in X-direction at the injection well are depicted. The resulting pressure gradient is defined as sum of these pressure gradients.

A characteristic flow velocity of injected  $\text{CO}_2$  can be calculated using the extended version of the Darcy's law for multiple phases. It has the form

$$v_\alpha = -\frac{k_{r\alpha}}{\mu_\alpha} \cdot \mathbf{K} \cdot \underbrace{(\nabla p_\alpha - \rho_\alpha \cdot \mathbf{g})}_I. \quad (4.9)$$

For the determination of the flow direction of the plume, the examination of the flow velocity in X-direction at the injection well is relevant and examined further, then.

Since a downwards movement is desirable, the resulting velocity should be smaller or equal to zero. This can only be the case, when the term I (see equation 4.9) of the Darcy's law is zero or less. This leads to following condition for a downwards movement of the plume:

$$\frac{\partial p_{\alpha}}{\partial x} - \sin(\alpha) \cdot \rho_{CO_2} \cdot g < 0. \quad (4.10)$$

The pressure gradient in X-direction, that was determined in equation 4.8 before, can be inserted into this condition (4.10), then. This gradient includes the formation water flow, the pressure due to buoyancy forces and the injection pressure. This extends inequation 4.10 to

$$\nabla P_{flow,x} + \nabla P_{grav,x} + \nabla P_{inj} - \sin(\alpha) \cdot \rho_{CO_2} \cdot g < 0 \quad (4.11)$$

Transformed and solved for the injection pressure, this leads to the condition, when the main propagation direction is down dip:

$$\nabla P_{inj,x} + \underbrace{\sin(\alpha) \cdot g \cdot (\rho_w - \rho_{CO_2})}_{\text{influence of buoyancy}} < -\nabla P_{flow,x} \quad (4.12)$$

When this condition is fulfilled, the occurring velocity at the injection well points in the downwards direction. The major flow direction of the plume will then also be in down dip direction. The last term in equation 4.12 describes the influence of buoyancy forces, referring to the density difference of the two fluids.

With this condition, a dimensionless pressure number can be created that describes the ratio of the pressure forces, that point in the up dip direction (positive X-direction) and the ones that point down dip. It compares the terms on both sides of inequation 4.12. It has the form:

$$Pr = \frac{\nabla P_{inj,x} + \sin \alpha \cdot g \cdot (\rho_w - \rho_n)}{P_{gw}/L} \quad (4.13)$$

Following estimations can be made:

Pr > 1	propagation in both directions or up dip
Pr < 1	propagation predominantly down dip

Table 4.3: Estimation of the flow direction

It can be used to estimate, at which injection pressures the carbon dioxide plume is pushed downwards by the groundwater flow. Different dip angles can be considered. The number shows to be a valid approximation for the performed simulations. Note that if the number is close to unity, no clear statement about the predominant propagation direction can be made, since other processes like capillary forces or relative permeabilities may have a greater influence then.

## 4.5 Subdivision of the Process into two Stages

When considering the output of the different model runs it becomes obvious that the process of CO<sub>2</sub> injection at the bottom of a dipped aquifer can be subdivided into two different stages:

- Stage I: Free movement, until the plume reaches the cap rock
- Stage II: Migration along the cap rock

### 4.5.1 Stage I: Free Movement

At the beginning of the injection, the plume can spread out freely into the aquifer. It is moving upwards due to buoyancy forces, which act in the opposite direction of the gravity vector, which is depicted according to the orientation of the model axes in figure 4.5. The propagation is at first not influenced by the geometry of the aquifer top. The shape of the plume is elliptic by then. This ellipsis is more or less skew upstream or downstream, depending on the formation water flow and the dip angle of the aquifer. The duration of this first phase depends on several parameters like the aquifer height, the dip angle, the vertical permeability, the density of the CO<sub>2</sub> phase and the depth of the aquifer.

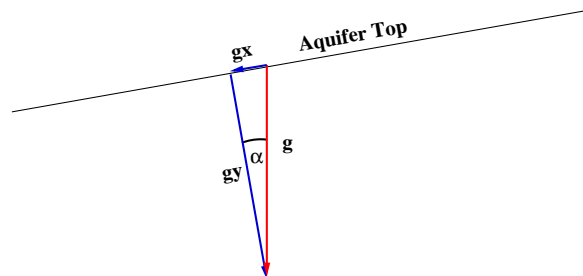


Figure 4.5: This figure describes the two components of the gravity vector considering the orientation of the model axes.

For the characterization of the free upwards movement during the injection, a dimensionless number is used to relate the mainly acting forces and to get a rough idea of the resulting plume evolution. These were identified as viscous and buoyancy forces. The suitability of different gravity numbers, which compare buoyancy forces to viscous forces to characterize this part of the plume behavior was tested, then. They should take into account as many of the varied parameters as possible. Moreover, the applied values should be unique and each of them should be only one value for the aquifer and the injection process. This means, that these values have to be characteristic and can subsequently be used to describe the flow behavior properly. The values that are used for the buoyancy numbers here are determined by the values that occur at the

injection point, since this determines the resultant behavior of the plume.

An overview of different more or less dimensionless gravity numbers can be found in Shook et al. [13]. Moreover, Van Lookeren [12] derived a dimensionless number from an analytical analysis of steam injection into an oil reservoir. It is a number, that describes the interface of a propagation front of steam and oil, relating to a mass flow into the system. Since many of the parameters, that were varied in the simulations, could be found in this number and it describes a similar process as CO<sub>2</sub> injection into a saline aquifer, it appears to be the helpful to describe the evolution of the shape. Note that the groundwater flow is not included in this number. However, it can be used as a dimensionless number, that compares buoyancy forces to viscous forces of the injection. With this, statements about the tendency of the plume to rise up to the cap rock and further up dip can be made. The number has the form:

$$A_{LD} = \frac{(\rho_w - \rho_n) \cdot \mathbf{g} \cdot h \cdot k_{r,n} \cdot \mathbf{K} \cdot \rho_n \cdot b}{\mu_n \cdot \dot{m}_n} \quad (4.14)$$

Moreover, the most common form of the gravity number (equation 4.15), derived from the decoupled pressure and saturation equations of a system (see research proposal by Kopp [11]), was considered:

$$Gr = \frac{(\rho_w - \rho_n) \cdot \mathbf{K} \cdot \mathbf{g}}{\mu_n \cdot v_{characteritic}} \quad (4.15)$$

When comparing those two dimensionless numbers, it becomes obvious that it is possible to transform the one number into the other and that they are similar but contain different variables. The Van-Lookeren number relates gravity forces that characterize buoyancy to viscous forces of the system. Since the two numbers were originally inverted to each other, the reciprocal value of the Van-Lookeren number is used and it becomes higher when the influence of buoyancy forces increases. Furthermore, the Van-Lookeren number refers to a characteristic mass flow, the other one refers to a characteristic velocity. A mass flow can be calculated from a velocity as follows:

$$\dot{m}_n = \rho_n \cdot v \cdot A \quad (4.16)$$

In this equation, A is the area, where the flow passes through with a (Darcy) velocity v and a density  $\rho_n$ . With this correlation, one number can be transformed into the other by inserting the velocity into the general form of the gravity number (4.15). Since they obviously include the same processes only differently expressed, the Van-Lookeren number was used further on. With this, the mass flow could be directly utilized in the number. The Van-Lookeren number is also referred to as buoyancy number in the following.

The parameters for this Van-Lookeren number for phase I are chosen as follows:

- The effective permeability  $K_{eff}$  is used. This is oriented with the gravity vector, as explained below.

- Viscosity and densities are calculated according to the aquifer temperature and pressure at the injection well.
- The mass flow was determined as 500 tons of injected CO<sub>2</sub> divided by the time that it took to inject this in the system.
- The area that occurs in the Van-Lookeren number is determined as the length of the injection well times the depth of the aquifer (here 1 m), indicating the area of injection (two-dimensional consideration).
- The relative permeability is set as constant to unity for this consideration.

Different simulation runs showed, that the mass flow rate can be seen as approximately constant with the constant pressure injection boundary and the applied parameters, although it slightly changes over time due to the influence of relative permeabilities. To illustrate this, the mass in the system and the calculated mass flow in the reference case is depicted in figure 4.6 over the respective time. This approximation can be made, if the influence of the relative permeabilities is moderate and the compressibility of the CO<sub>2</sub> is low, e.g. when it is in a liquid or supercritical state.

For the determination of the mass flow rates of the different cases, the point in time, when the plume reaches the before mentioned balance line which is situated 500 meters down dip the injection, was chosen, in order to have a comparable value for the different simulations. Moreover, this was compared to the mass flow rate that can be calculated when 500 tons of carbon dioxide are injected into the reservoir. Small differences could be observed, depending on the varied parameter. But for the consideration here, these differences can be neglected.

When considering anisotropic aquifers, the used permeability in the buoyancy number should point in direction of the acting gravity vector. Usually, the anisotropies occur perpendicular to the aquifer geometry. Thus, an effective permeability in direction of the gravity vector is calculated, taking into account the dip angle of the aquifer. Equation 4.19 describes the calculation of the vertical permeability further. The resulting vertical permeability of an anisotropic medium with a lower permeability in Z-direction becomes larger, when the dip angle increases.

$$\vec{g} \cdot \vec{K} = \begin{pmatrix} g \cdot \sin \alpha \\ g \cdot \cos \alpha \end{pmatrix} \cdot \begin{pmatrix} K_{xx} & 0 \\ 0 & K_{zz} \end{pmatrix} \quad (4.17)$$

$$= g \cdot (\sin \alpha \cdot K_{xx} + \cos \alpha \cdot K_{zz}) \quad (4.18)$$

Consequently, the effective permeability can be calculated by following equation:

$$K_{eff} = \sin(\alpha) \cdot K_{xx} + \cos(\alpha) \cdot K_{zz}. \quad (4.19)$$

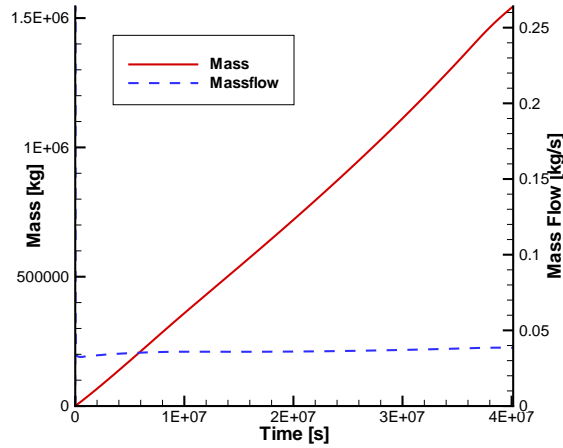


Figure 4.6: The mass flow for the Reference case over time is depicted. The supercritical cases showed all a similar quasi-linear behavior of the mass flow. However, this was not true for gaseous  $\text{CO}_2$  due to the compressibility.

With this massflow and with the calculated effective permeability, it is possible to calculate the Van-Lookeren number and to examine the ratio of the acting forces. With their help, the influence on the plume evolution can be estimated. The reference case was subsequently compared with different parameter variations, to get an idea of the impact of the respective parameter change. The Van-Lookeren number is then used as an indicator, whether the gravitational forces or the viscous forces dominate the system. Strong gravitational forces promote a faster arrival of the plume at the cap rock and a stronger up dip propagation of the injected  $\text{CO}_2$ .

The pressure ratio described before gives a good approximation of the dominating flow direction. Phase one ends, when the plume reaches the cap rock. This phase has little influence on the evolution behavior, when the aquifer height is very low and the vertical permeability is high.

### 4.5.2 Stage II: Migration Along the Cap Rock

Stage two describes the assimilation and lateral migration of the plume along the cap rock. This stage has to be examined slightly differently as the first stage and the used values for the Van-Lookeren number are different. Buoyancy forces perpendicular to the cap rock have little influence on the shape of the plume, and so the important part of the gravity vector is reduced to the one parallel to the cap rock. This is proportional to the sinus of the dip angle of the aquifer, as described below. Consequently, larger dip angles lead to a higher tendency of the plume, to develop in the up dip direction.

The part of the gravity vector that has an effect on the development of the plume shape close to the cap rock can be reduced to the X-component:

$$\vec{g} = \begin{pmatrix} g \cdot \sin(\alpha) \\ 0 \end{pmatrix} \quad (4.20)$$

Moreover, only the permeability in X-direction needs to be considered here, because the Z-component disappears when the gravity vector of equation 4.20 is multiplied by the permeability tensor. Additionally, the saturations at the cap rock increase more and more. This has the effect, that the relative permeability is getting higher in that region as well. Subsequently, this promotes that the CO<sub>2</sub> phase flows further along the cap rock, preferably there, where a high relative permeability already exists. This leads to the fact, that the predominant flow direction, that was estimated with the help of the pressure number, does not switch after reaching the cap rock and so the pressure number gives valuable information here as well.

The CO<sub>2</sub> phase must migrate laterally along the cap rock and the plume begins to spread. Without dip and groundwater flow, it would spread equally into both directions. But due to the dip angle, the X-component of the gravity vector forces an upwards movement of the CO<sub>2</sub>. This is one reason, why the plume is distributed unproportionally then. A preferred flow path can form, which rises further up dip, if the groundwater flow is not strong enough to prevent this.

The Van-Lookeren number is then determined as

$$A_{LD} = \frac{\sin(\alpha) \cdot g \cdot (\rho_w - \rho_n) \cdot A \cdot k_{r,n} \cdot K_{xx} \cdot \rho_n}{\mu_n \cdot \dot{m}_n}. \quad (4.21)$$

Moreover, since buoyancy has only an effect in X-direction, the permeability in X-direction ( $K_{xx}$ ) is used for the calculation of the Van-Lookeren numbers. The parameters for the Van-Lookeren number for stage II are summarized in the following list:

- The gravity vector is reduced to its X-component ( $\sin(\alpha) \cdot g$ ).
- The intrinsic permeability in X-direction is used ( $K_{xx}$ ).
- Viscosity and densities are also calculated according to the aquifer temperature and pressure at the injection well.
- The determination of the mass flux is the same as in phase I.
- The relative permeability is set as constant to unity for this consideration.

The buoyancy numbers of the two stages can be used to examine the relation of the acting forces in the respective phase. The number of stage I describes the ratio of buoyancy to the advective forces of the injection, the other one relates the gravity forces, that act at the cap rock to the advective forces there. It is an indicator for the tendency of the CO<sub>2</sub>, to migrate upwards along the cap rock. In the performed simulations, the vertical extend of the aquifers is much lower as the horizontal. Thus, stage two is more important here.

## 4.6 Mass Distribution in the Aquifer

In order to quantify the spatial distribution of the injected CO<sub>2</sub>, the ratio of the mass distribution within the aquifer was determined. This was done by subdividing the domain into two halves by a line rectangular to the midpoint of the aquifer top and bottom, crossing in the middle of the injection well. Then, the mass within each sub domains was determined. A mass ratio was calculated, relating the CO<sub>2</sub> mass in the part upstream the well to the mass in the down dip part. When this ratio equals one, the distribution is equal in both sub domains. Smaller values indicate that the predominant part of the injected CO<sub>2</sub> is in the lower half of the aquifer. Note that the mass ratio does not equal zero, even when all of the injected CO<sub>2</sub> flows downwards. This is because the aquifer was divided in the middle and parts of the injection well are in the up dip part.

The mass ratio changes over time. To make the different models comparable, a characteristic point in time had to be chosen at which the ratio is determined. Therefore, the arrival time of the CO<sub>2</sub> at a distance of 500 meters downstream the well was chosen, so that the plume can develop and is still far enough from the model boundaries away. This mass ratio is called *Ratio* in the further analysis. To examine the influence of the chosen point in time on this ratio, two other points in time were chosen to compare the mass ratios:

- the point in time, when 500 tons of CO<sub>2</sub> were in the system (Ratio500)
- the point in time, when the minimum mass ratio occurred (Ratiomin)

The last ratio (Ratiomin) was not always applicable, since not all simulations showed a minimum in the development of the ratio over time, especially when the plume migrates upwards. The three different mass ratios that were determined have a comparable behavior in the performed simulations.

## 4.7 Parameter Variation

In the following, single parameters were varied while the others of the reference case were kept constant in order to see the effect of each parameter. The influence of these parameters on the evolving shape of the plume is examined with the help of the mass ratio, the two forms of the Van-Lookeren number and the pressure number. An overview of the values that were used in the different cases can be found in table 4.18 at the end of the chapter. The calculated gravity numbers, mass ratios and pressure numbers are listed in table 4.19

### 4.7.1 Variation of the Aquifer Depth

As mentioned earlier, the aquifer depth has an influence on the predominant pressure, temperature and subsequently on densities and viscosities of the fluids. The simulations had to be adjusted, in order to have a comparable injection rate. The different aquifer depths lead to different densities of the injected CO<sub>2</sub>. Since the density of gaseous CO<sub>2</sub> is much lower than the one of supercritical CO<sub>2</sub> and compressibility of the gas phase plays a role, much less CO<sub>2</sub> is entering the aquifer, when the same injection pressure is applied. To partly blend out this effect, the injection pressure was adjusted for the shallow cases. Due to the compressibility of gaseous CO<sub>2</sub>, the density of the injected CO<sub>2</sub> increases and suitable injection pressures are not easy to determine. With this, the correlation between injection pressure and CO<sub>2</sub> mass flow into the system is becoming non-linear. In the deeper cases, the adjustment of the injection pressure was not necessary because the pressure change to the absolute pressure and consequently the density change is negligible. There, an approximately linear correlation of injection pressure and mass flow could be observed.

Moreover, for the calculation of the Van-Lookeren number, the viscosities and densities were chosen according to the respective pressure at the injection point. They take also the additional pressure of the groundwater flow and of the injection into account and represent the values at the injection well.

To capture the effect of injecting in different depths, the depth of the reservoir was varied in a range from 350 meters, where the injected CO<sub>2</sub> is in a gaseous state, to 1500 meters, where it is a supercritical fluid. In the cases of storage into shallow depths, CO<sub>2</sub> has very low densities and viscosities. The propagation velocity is very fast then and the cap rock is reached very quickly. Moreover, due to the low density and viscosity, the tendency to escape the storage aquifer is strong.

Two examples with the same mass injected into the system are shown in the following figures:

When getting deeper than 700 meters, the CO<sub>2</sub> phase is in a supercritical state and its density and viscosity is much higher than before. This affects buoyancy and the propagation behavior in a way, that the propagation velocity is slower and buoyancy forces become remarkably weaker.

This is partly reflected in the Van-Lookeren number. Its development is depicted in figure 4.8 (a). In depths less than 700 meters, this number increases with increasing depth. One would expect, that the Van-Lookeren number in low depths is very high, indicating that the buoyancy forces are strong in comparison to the viscous forces. The graph shows a different behavior. If the Van-Lookeren number is considered closer, the reason can be seen. The buoyancy forces are indeed stronger, because the density difference in the dimensionless number is becoming larger. But, when the mass flow rate is kept constant, the viscous forces are becoming stronger as

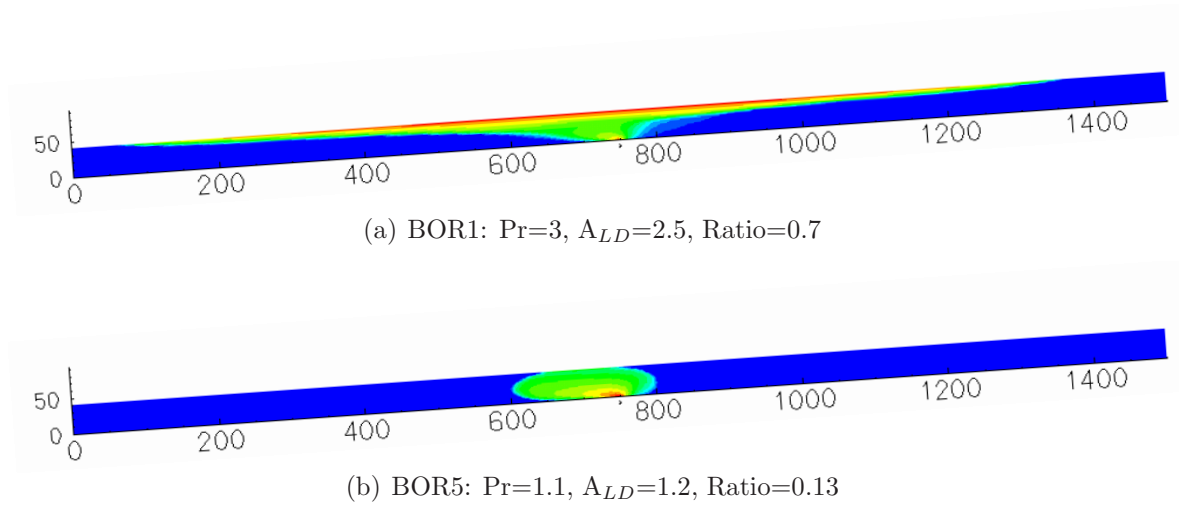


Figure 4.7: Saturation profiles after injection of 350 t/m CO<sub>2</sub> into a depth of 350 meters (a). The plume shows a strong tendency to move upwards due to strong buoyancy forces. Viscosity of the CO<sub>2</sub> phase is very low. Injection of 350 t/m CO<sub>2</sub> into a depth of 1500 meters (b). Here, the plume is much more compact and the tendency to rise to the cap rock is weaker. The viscosity of the CO<sub>2</sub> phase is much higher than in the shallow case.

well. The density of the CO<sub>2</sub> decreases, when the mass flux is kept constant and the injection is situated in a lower depth. As a result, the velocity of the CO<sub>2</sub> flow is getting considerably higher. The velocity is proportional to the viscous forces. Subsequently, these forces increase when density is lower and the same mass rate is injected.

This increase of the viscous forces influences the Van-Lookeren number stronger than the rise in the buoyancy force. Moreover, the dynamic viscosity ( $\mu_n$ ), that occurs in the denominator of the Van-Lookeren number, has a similar behavior as the density in the nominator, when the aquifer depth is changed. The ratio of the CO<sub>2</sub> density to the viscosity is depicted in figure 4.8. The development of this ratio has also a strong influence on the Van-Lookeren number.

The ratio of the acting forces changes considerably, when the state of aggregation of the CO<sub>2</sub> changes. In depths greater than 700 meters (supercritical state) the Van-Lookeren number decreases with increasing depth, indicating that the influence of buoyancy is becoming lower, then.

The pressure number is becoming smaller in deeper aquifers. This is reflected in the developing of the mass distribution in the aquifer. The plume has a stronger tendency to move down dip, when the depth of the injection is situated deeper. This is depicted in figure 4.8(b).

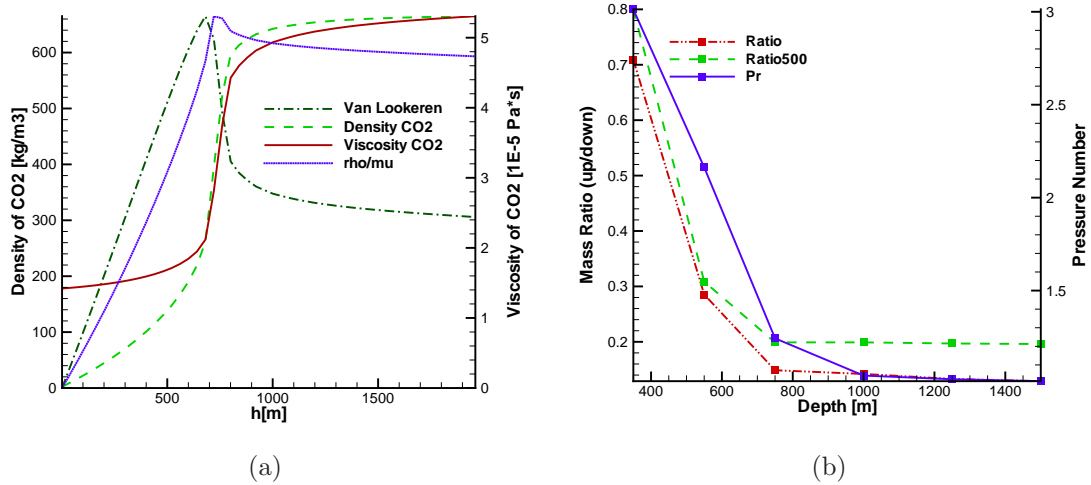
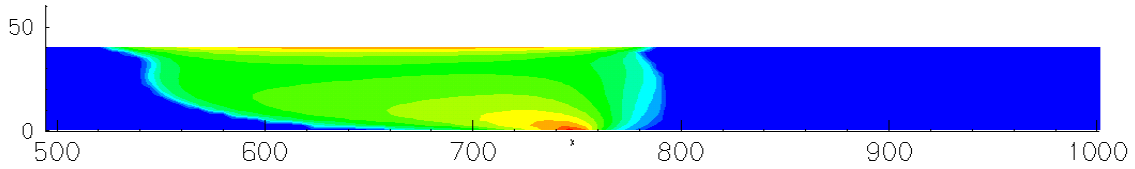
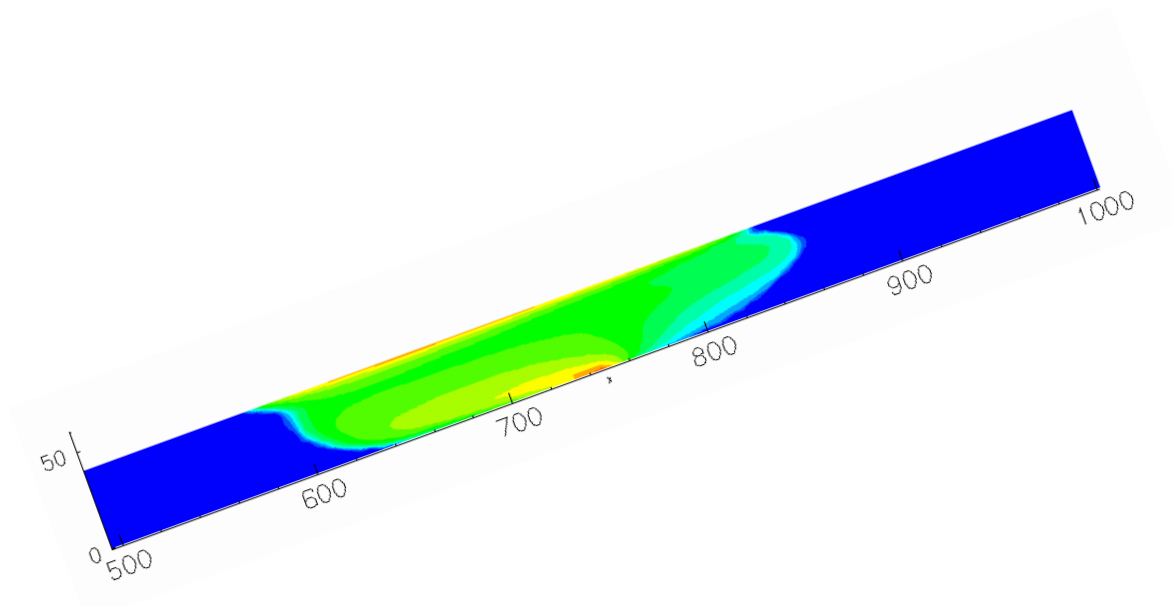


Figure 4.8: Figure (a) depicts the Van-Lookeren number with depth. The dynamic viscosity and density of CO<sub>2</sub> and the ratio of these two properties are included in this figure. This shows, the influence of this ratio on the Van-Lookeren number. Figure (b) shows the pressure number and the mass ratio with depth. The curves show a similar behavior.

### 4.7.2 Variation of the Dip Angle



(a) Dip0:  $Pr=0.5$ ,  $A_{LD}=0.1$ , Ratio=0.11



(b) Dip6:  $Pr=3.16$ ,  $A_{LD}=8.1$ , Ratio=0.52

Figure 4.9: Saturation profiles after injection of 500 tons  $CO_2$  with a dip angle of  $0^\circ$  (a) and  $20^\circ$  (b)

The dip angle of the aquifer has an influence on the propagation behavior and on the shape evolution of the plume. When the injection is not situated directly under the cap rock, the  $CO_2$  can first freely move and rise up to the cap rock (stage I). The dip angle of the aquifer has an effect on the skewness of the propagation, because the direction of the undisturbed water gradient and the resulting flow depends on the dip angle.

When the cap rock is reached, the plume spreads and migrates along the confining cap rock. The upwards directed part of the buoyancy force is then promoting an upwards migration, as described before. This part of the buoyancy force is proportional to the sinus of the dip angle and to the relative permeability that is reached there. Thus, the influence of buoyancy on the shape is becoming stronger with a larger dip angle. This can be seen when considering the pressure number and the resulting mass ratios of the simulations. They show an almost linear coherence (see figure 4.10 (a)).

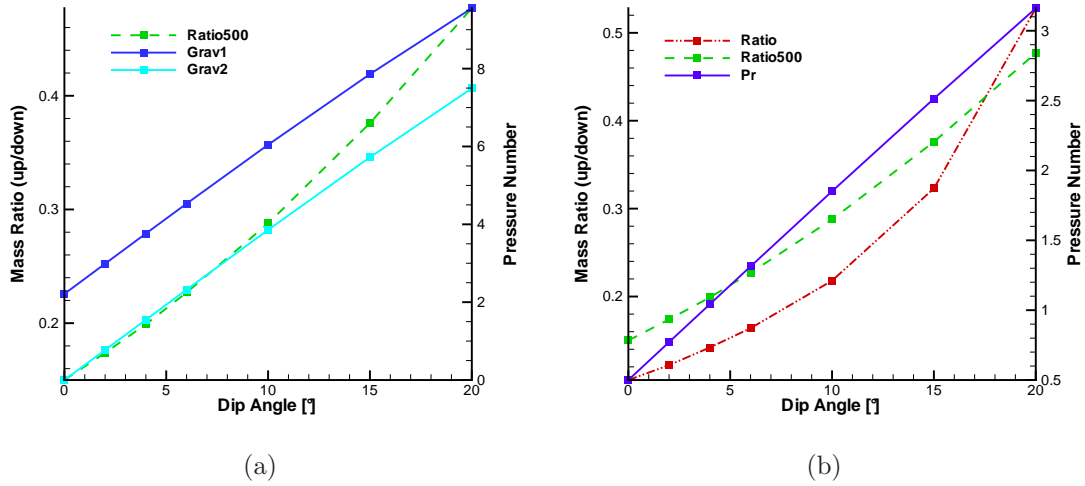


Figure 4.10: Figure (a) shows the development of the Van-Looken Numbers (Grav1 for stage I and Grav2 for stage II) with the dip angle of the aquifer. A larger dip angle leads to a stronger tendency of the plume to rise up dip. This is reflected in the pressure number and the mass distribution. Figure (b) shows the coherence of the dip angle with the pressure number and the resulting mass distributions.

The relation of the Van-Looken number and the dip angle of the aquifer is depicted in figure 4.10(b). In the first stage, the gravity number is influenced only by the resulting permeability, which becomes higher with the dip angle, if an anisotropic aquifer is considered. When the cap rock is reached, the gravity number is different because buoyancy can only act along the cap rock from then on. Subsequently, the permeability in X-direction is used (stage II) and the X-component of the gravity vector is applied. The development of the two numbers is depicted in figure 4.10(a).

The cases with a lower dip angle than the reference case show only little differences. But when the dip angle increases, the plume is shifted upwards. Moreover, the angle of the gravity vector and the water flow vector is not perpendicular anymore. In the latter case of a dip angle of 20 degrees, the upwards driving forces are stronger than the groundwater flow and the CO<sub>2</sub> takes its way upwards along the cap rock. This can be seen in figure 4.9(b), which depicts the resulting saturation profile after 500 tons carbon dioxide are injected.

### 4.7.3 Variation of the CO<sub>2</sub> Injection Pressure

The injection pressure has a strong effect on the pressure distribution within the reservoir. This is taken into account in the pressure number. When the injection starts, the pressure build-up is taking place into all directions. This leads to an alteration of the pressure isolines. Moreover, the mass flow is approximately proportional to the injection pressure. This is shown in figure 4.13.

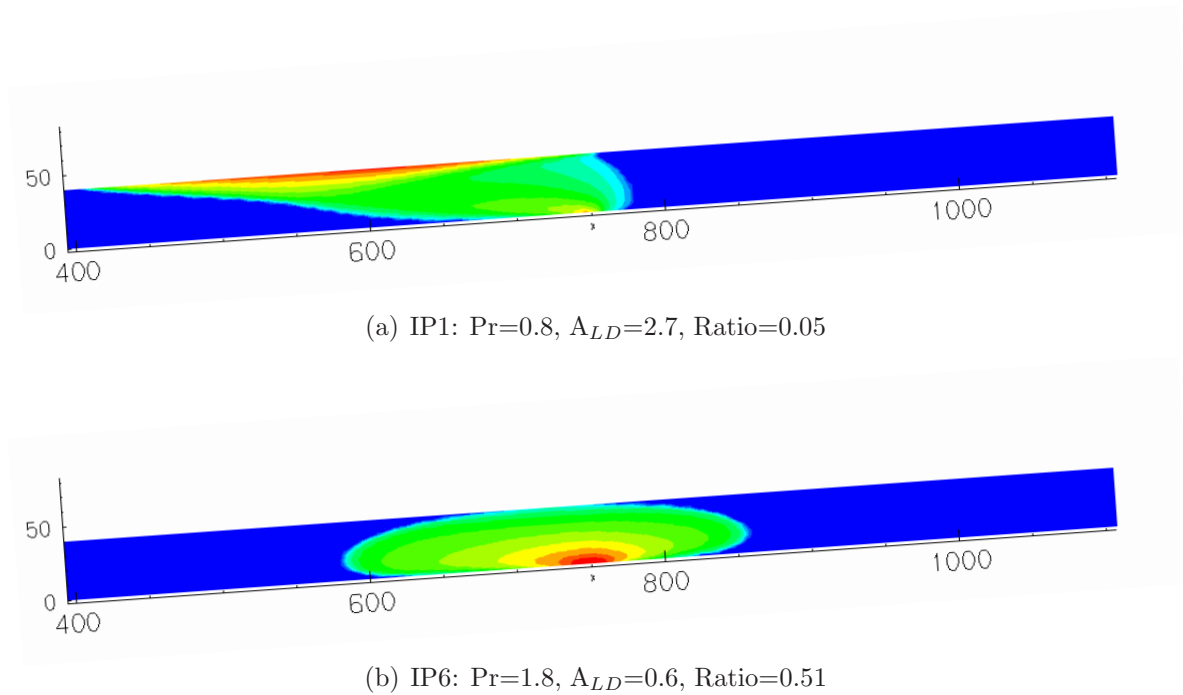


Figure 4.11: Saturation profiles after an injection of 500 t/m with an injection pressure of  $2E5$  Pa (a) and  $10E5$  Pa (b). The shape of the plume in figure (b) is more compact and the propagation is less influenced by the groundwater flow.

As described before, the injection pressure has to be considered simultaneously with the water flow pressure and the buoyancy force, since these pressures are interacting. The gravity number and the pressure number are strongly affected by the alternation of the injection pressure. Figure 4.12 (a) shows the development of the Van-Looken number with different injection pressures. The viscous forces increase due to higher injection pressures, which produce higher propagation velocities of the CO<sub>2</sub> phase, while the buoyancy forces remain relatively unaffected, when the CO<sub>2</sub> is in a supercritical state.. Thus the Van-Looken number becomes lower with increasing pressure.. The development of the pressure number with different injection pressures can be seen in figure 4.12(b). The mass ratio ( $Ratio$ ,  $Ratio500$ ) is becoming bigger with higher injection pressures, indicating a stronger movement up dip.

Two simulations with the pressure number smaller than one and greater than unity

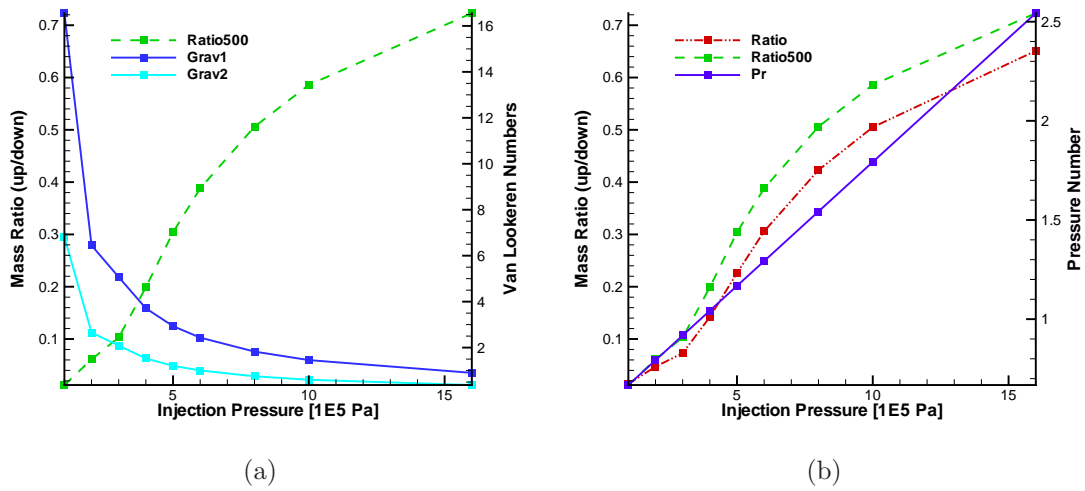


Figure 4.12: Figure (a) depicts the development of the Van-Lookenren number with the injection pressure. Higher injection pressures lead to lower buoyancy numbers due to the increase of the viscous forces. Figure (b) shows the mass distribution and pressure number with different injection pressures. The mass ratio shows a good coherence with the pressure number.

are shown in the two figures 4.11. The saturation profiles show the distribution of the  $\text{CO}_2$  saturation with the same mass in the system. They show, that if the same mass is injected with a lower injection rate, the predominant propagation direction is shifted down dip. Moreover, the influence of buoyancy forces is less.

Figure 4.13 shows the behavior of the mass flow, when only the injection pressure is changed. It shows an almost linear coherence, when the carbon dioxide is in a supercritical state.

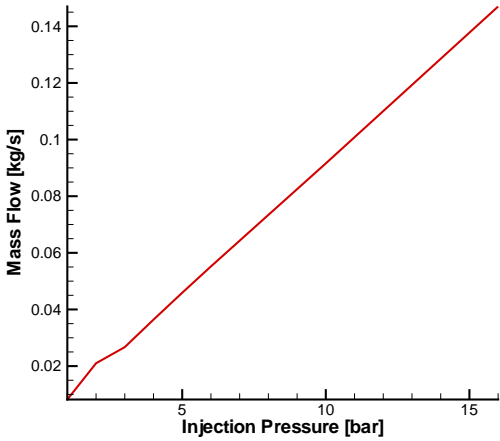


Figure 4.13: Mass Flow with Different Injection Pressures. This curve shows, that the relation can be seen as constant in the supercritical state. However, due to the influence of compressibility, this is can not be assumed for CO<sub>2</sub> in a gaseous state.

#### 4.7.4 Variation of the Ambient Formation Water Flow

At first, a simulation run without water flow was performed, in order to get an idea of the undisturbed propagation of the plume. Therefore, the reference model was used with the water flow pressure  $P_{flow}$  at the east boundary set to zero. An up dip rise of the plume could be observed. Then, different pressures were applied at the east boundary.

The water flow down dip the aquifer has the effect that the plume of the CO<sub>2</sub>-phase is shifted downwards (friction forces between the phases are not taken into account) and dissolved CO<sub>2</sub> is transported with the flow. The stronger the formation water flow is, the more is the propagation direction of the CO<sub>2</sub> shifted downwards. This can even outrange the buoyancy of the lighter CO<sub>2</sub> phase.

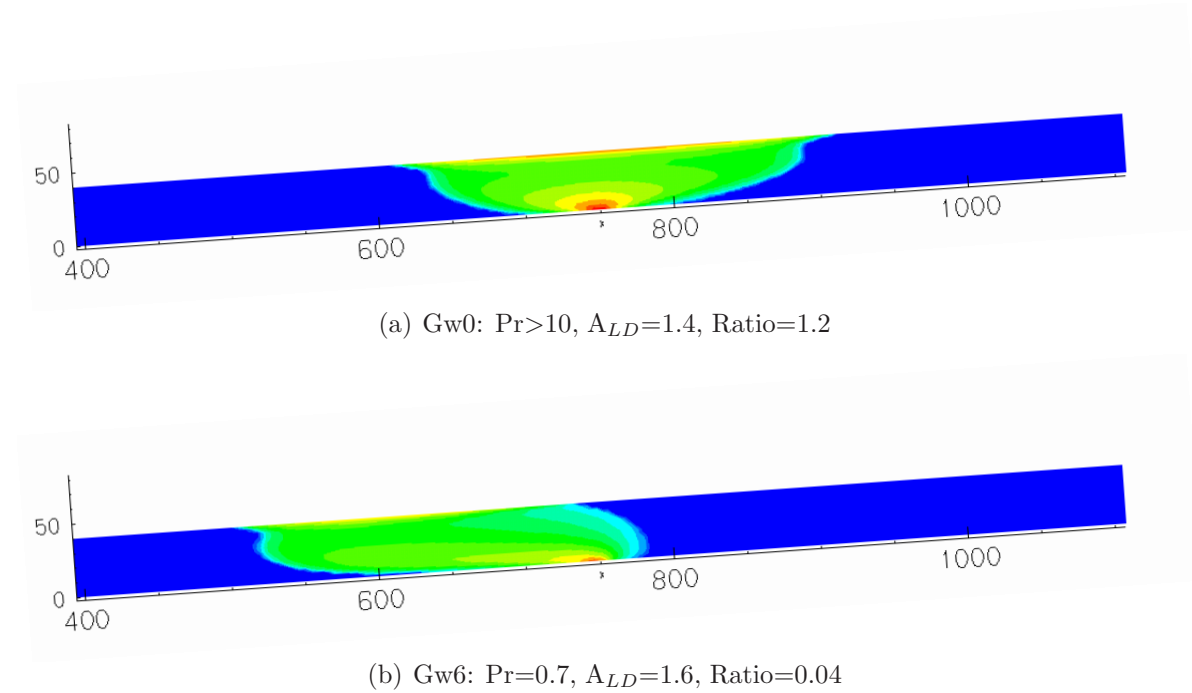


Figure 4.14: Saturation profile after injection of 500 t/m CO<sub>2</sub> with no formation water Flow (a) and a strong water flow with a flow pressure at the east boundary of 12E5 Pa. The plume is shifted downwards by the water flow.

Since the mass flow of brine is not taken into consideration in the Van-Lookeren number, it does not change with different formation water flow rates and no conclusion can be made. But the pressure number is strongly affected by the influence of the water flow and gives a good estimation of the flow direction and the resulting mass distribution of the CO<sub>2</sub> plume, as can be seen in figure 4.15. The simulations also show, that the flow pressure has to be relatively strong in order to enforce a downwards propagation.

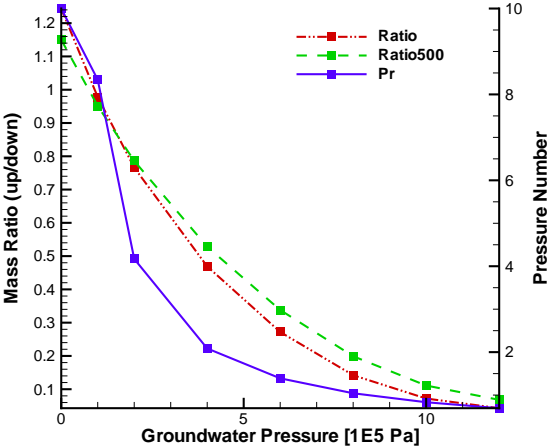
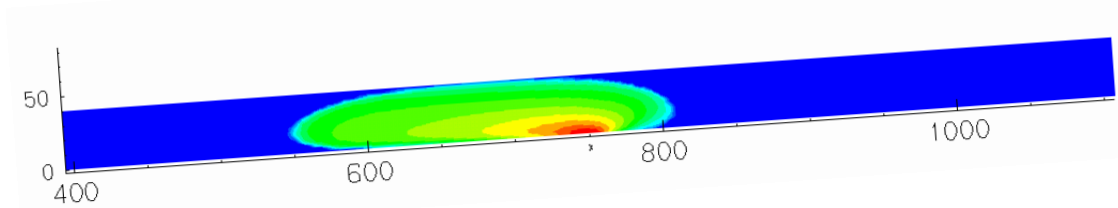


Figure 4.15: Development of the mass distribution and the pressure number with the water flow pressure.

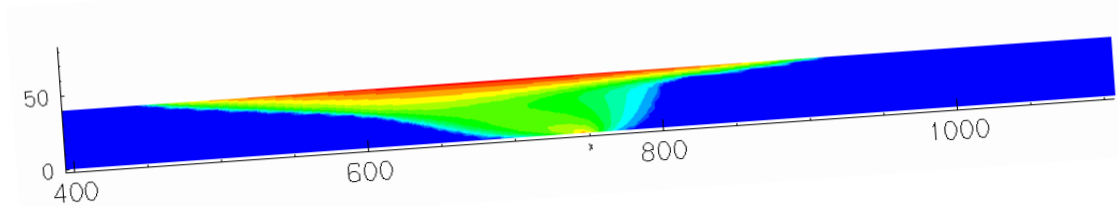
### 4.7.5 Variation of the Intrinsic Permeability

When considering the setup with different permeabilities, it becomes obvious that the injection rates and the formation water flow changes proportional to the intrinsic permeability. To have a comparable injection rate, the injection pressure of the CO<sub>2</sub> was adjusted then, so that the mass flow into the system was the same. The water flow pressure was adapted accordingly. That means, that the absolute value of the groundwater pressure was changed in relation to the injection pressure. So, a constant mass flow and flow velocity into the system could be obtained.

The results show, that the intrinsic permeability has a strong influence on the propagation behavior. In aquifers with a low intrinsic permeability, the shape of the plume is rather compact, whereas in aquifers with a high permeability the plume can migrate fast. The cap rock is reached soon and the plume begins to spread, there.



(a) P2: Pr=0.8,  $A_{LD}$ =0.8, Ratio=0.12



(b) P4: Pr=1.3,  $A_{LD}$ =2.3, Ratio=0.19

Figure 4.16: Saturation profile, when 500 t/m CO<sub>2</sub> are injected into an aquifer with a low horizontal permeability of 0.5E-12 m<sup>2</sup> (a) and one with a high horizontal permeability of 1.5E-12 m<sup>2</sup> (b).

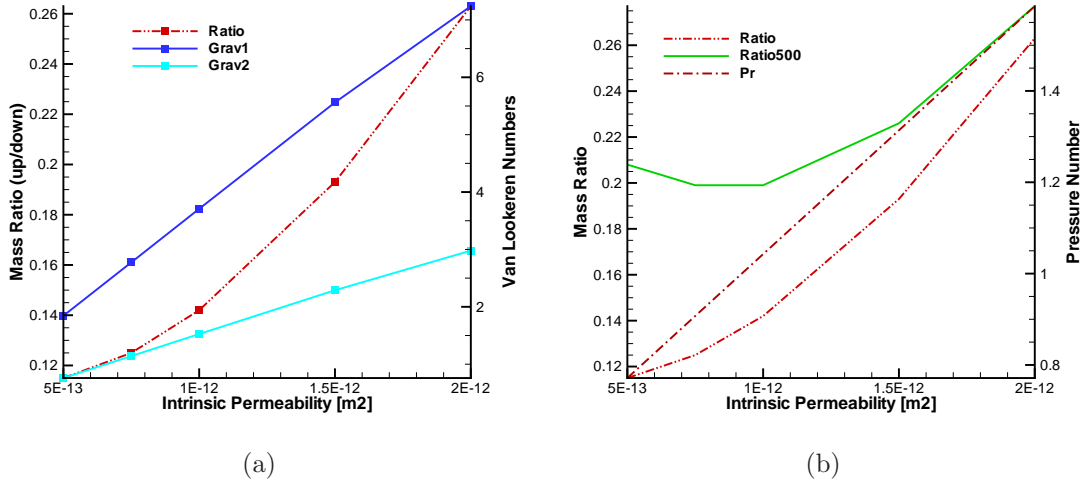


Figure 4.17: Figure (a) depicts the development of the Van-Lookeren numbers (Grav1, Grav2) with different permeabilities. Moreover, the resulting mass ratio is shown. Figure (b) shows the mass ratio and pressure number with different permeabilities.

## 4.8 Results

The simulations and the consideration of the pressure ratios and Van-Lookeren numbers show the influence of the different parameters. Parameters that are determined as favorable for a down dip propagation of CO<sub>2</sub>, which is injected in a dipped aquifer including a formation water flow in down dip direction, are:

- a strong groundwater flow
- a high injection depth (deeper than 700 meters) resulting in a high CO<sub>2</sub> density
- low injection rates
- low permeabilities
- a low dip angle of the aquifer

Interfacial friction between the brine- and the CO<sub>2</sub> phase and potentially occurring bubbling or fingering (formation of a preferred flow path) are not taken into account in the applied form of the MUFTE-UG code. This may also influence the propagation behavior.

To get clarity about further effects like dissolution or the behavior of the groundwater flow like dodging around the injected plume, different 3D simulations were performed using real data. It is interesting to see if the CO<sub>2</sub> is taking a path upwards and

the surrounding water dodges around it and flows downwards there. Moreover, the suitability of a certain site is tested.

The examination of the different simulations showed that the injection of carbon dioxide into a dipped aquifer with a groundwater flow is a highly complex process, which cannot be described with a single dimensionless number. However, at least a set of several different numbers would be needed for a classification of the described process. This shows the importance of performing numerical simulations. However, dimensionless numbers can be used to get a better understanding of the processes that occur and to do some rough estimations about the expected behavior.

Name	DOI [mbsl]	Dip Angle [°]	Pinj [1E5 Pa]	Pgw [1E5 Pa]	K_x [m <sup>2</sup> ]
BOR1	350	4	14	8	1.0E-12
BOR2	550	4	8	8	1.0E-12
BOR3	750	4	4	8	1.0E-12
REF	1000	4	4	8	1.0E-12
BOR4	1250	4	4	8	1.0E-12
BOR5	1500	4	4	8	1.0E-12
Dip0	1000	0	4	8	1.0E-12
Dip2	1000	2	4	8	1.0E-12
REF	1000	4	4	8	1.0E-12
Dip3	1000	6	4	8	1.0E-12
Dip4	1000	10	4	8	1.0E-12
Dip5	1000	15	4	8	1.0E-12
Dip6	1000	20	4	8	1.0E-12
IP0	1000	4	1	8	1.0E-12
IP1	1000	4	2	8	1.0E-12
IP2	1000	4	3	8	1.0E-12
REF	1000	4	4	8	1.0E-12
IP3	1000	4	5	8	1.0E-12
IP4	1000	4	6	8	1.0E-12
IP5	1000	4	8	8	1.0E-12
IP6	1000	4	10	8	1.0E-12
IP7	1000	4	16	8	1.0E-12
Gw0	1000	4	4	0	1.0E-12
Gw1	1000	4	4	1	1.0E-12
Gw2	1000	4	4	2	1.0E-12
Gw3	1000	4	4	4	1.0E-12
Gw4	1000	4	4	6	1.0E-12
REF	1000	4	4	8	1.0E-12
Gw5	1000	4	4	10	1.0E-12
Gw6	1000	4	4	12	1.0E-12
P2	1000	4	8	16	5.0E-13
P3	1000	4	5.33	10.66	7.5E-13
REF	1000	4	4	8	1.0E-12
P4	1000	4	2.66	5.33	1.5E-12
P5	1000	4	2	4	2.0E-12

Figure 4.18: This table shows an overview of the values that were used in the different simulation runs. DOI is the depth of injection.

Name	Ratio	Ratio500	Ratiomin	Lookeren1	Lookeren2	Pr
<b>BOR1</b>	0,71		0,70	6,06	2,50	3,01
<b>BOR2</b>	0,29	0,31	0,26	6,42	2,64	2,16
<b>BOR3</b>	0,15	0,20	0,11	4,65	1,91	1,24
<b>REF</b>	0,14	0,20	0,11	3,71	1,53	1,04
<b>BOR4</b>	0,13	0,20	0,10	3,28	1,35	1,02
<b>BOR5</b>	0,13	0,20	0,10	2,97	1,22	1,01
<b>Dip0</b>	0,11	0,15	0,07	2,15	0,00	0,50
<b>Dip2</b>	0,12	0,17	0,09	2,93	0,76	0,77
<b>REF</b>	0,14	0,20	0,11	3,71	1,53	1,04
<b>Dip3</b>	0,16	0,23	0,13	4,51	2,31	1,31
<b>Dip4</b>	0,22	0,28	0,21	6,49	4,14	1,85
<b>Dip5</b>	0,32	0,38	0,32	8,30	6,04	2,51
<b>Dip6</b>	0,53	0,48	0,43	10,27	8,06	3,16
<b>IP0</b>	0,01	0,01	0,01	16,55	6,81	0,67
<b>IP1</b>	0,05	0,06	0,03	6,45	2,65	0,79
<b>IP2</b>	0,07	0,10	0,04	5,07	2,09	0,92
<b>REF</b>	0,14	0,20	0,11	3,71	1,53	1,04
<b>IP3</b>	0,23	0,30	0,19	2,93	1,21	1,17
<b>IP4</b>	0,31	0,39	0,27	2,43	1,00	1,29
<b>IP5</b>	0,42	0,51	0,39	1,82	0,75	1,54
<b>IP6</b>	0,51	0,59	0,48	1,45	0,60	1,79
<b>IP7</b>	0,65	0,72	0,63	0,90	0,37	2,54
<b>Gw0</b>	1,24	1,15		3,30	1,36	
<b>Gw1</b>	0,98	0,95	0,94	3,39	1,40	8,34
<b>Gw2</b>	0,77	0,79	0,76	3,51	1,44	4,17
<b>Gw3</b>	0,47	0,53	0,46	3,56	1,47	2,09
<b>Gw4</b>	0,27	0,34	0,24	3,64	1,50	1,39
<b>REF</b>	0,14	0,20	0,11	3,71	1,53	1,04
<b>Gw5</b>	0,07	0,11	0,04	3,78	1,56	0,83
<b>Gw6</b>	0,04	0,07	0,02	3,90	1,61	0,70
<b>P2</b>	0,12	0,21	0,07	1,84	0,76	0,77
<b>P3</b>	0,13	0,20	0,09	2,77	1,14	0,91
<b>REF</b>	0,14	0,20	0,11	3,71	1,53	1,04
<b>P4</b>	0,19	0,23	0,17	5,56	2,29	1,31
<b>P5</b>	0,26	0,28	0,26	7,24	2,98	1,59

Figure 4.19: This table shows an overview of the calculated dimensionless numbers and mass ratios that were determined in the simulations. Lookeren1 is the Van-Lookeren number in the first stage (before reaching the cap rock), Lookeren2 describes the second stage.

# Chapter 5

## 3D Simulations

In the second part of this thesis, a certain site is examined with the help of three-dimensional numerical models using real world data. This is an investigation, if it is feasible to store CO<sub>2</sub> into a dipped aquifer at a site with given conditions and a formation water flow in the down dip direction. Moreover, some effects like dissolution of CO<sub>2</sub> in brine, which are not correctly represented in 2D, can be examined here. The underlying data was kindly provided with the request of not announcing neither the provider nor the exact location of the examined site.

### 5.1 Aquifer Parameters and Simulation Setup

The dipped aquifer top is situated in a depth between 90 and 170 meters below sea level. Its intrinsic permeability is significantly lower (several orders of magnitude) than the one of the storage aquifer, which has an horizontal permeability of 1E-12 m<sup>2</sup>. It has an average dip angle of 3 degrees. The rough edge length of the approximately rectangular model area amounts to 1950 meters. In total, the horizontal area sums up to 3.8 km<sup>2</sup>. Since no clear data about the aquifer bottom is available, the layer is assumed to have a constant thickness of 250 meters. This value is used, because clay could be observed 250 meters below the aquifer top in drilling cores. This was not the case above and may be an indicator for the beginning of a new layer or at least one with a different composition.

With this thickness, the deepest point in the model area is situated 420 meters below sea level. The aquifer bottom is also set as impermeable, since the injected CO<sub>2</sub> rises upwards due to strong density differences and, moreover, a layer with a lower permeability follows downwards. Thus, the lower parts are not important for the plume propagation. The storage aquifer is situated in a zone with two different permeability ranges. The first model runs were performed with a constant horizontal permeability of 1E-12 m<sup>2</sup>. Later on, the permeability distribution within the aquifer was subdivided into two zones with different permeabilities.

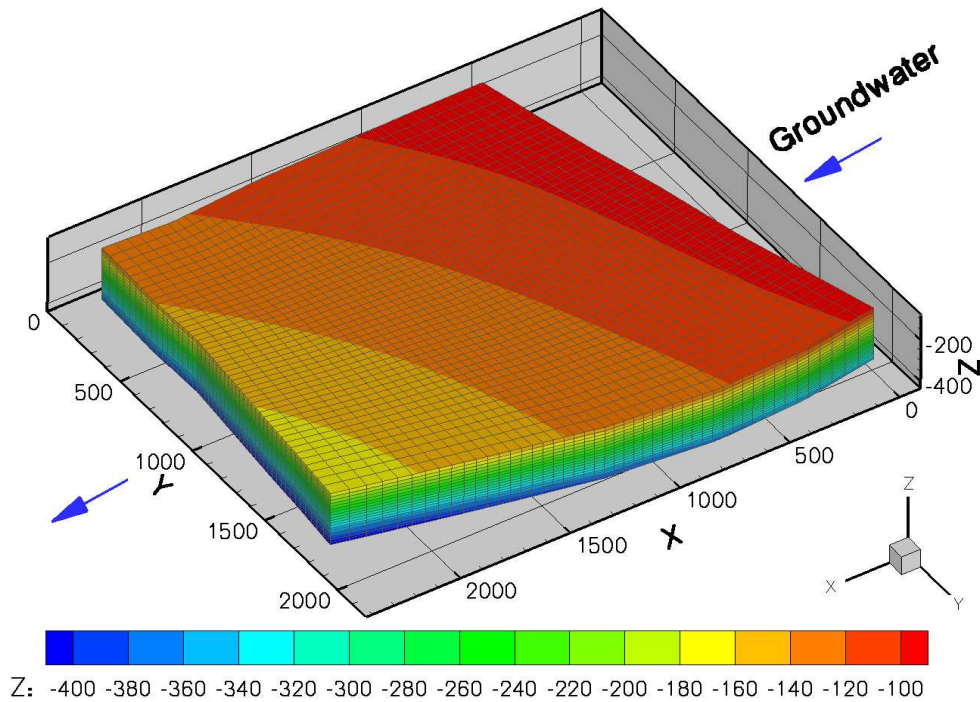


Figure 5.1: View on the aquifer showing the depth of the aquifer. Moreover, the contours of the grid and the orientation of the axes is displayed.

Figure 5.1 shows the aquifer from top view. The colors represent the depth below sea level of the upper aquifer limits, indicating a decline from the upper right to the lower left side of the aquifer. The formation water flow takes place in positive X-direction. The ambient water flows down dip within the aquifer with an approximate velocity of  $1E-7$  meters per second. The water flow direction is shown by stream traces in figure 5.3. The injection well is placed into the middle of the reservoir, at the coordinates  $X = 1270.65$  m and  $Y = 959.6$  m. It is assumed that the injection takes place in the lowest 23 meters of the aquifer, in a depth from -349 m to -372 m below sea level. This represents a screened well, which is closed in the upper parts of the reservoir.

### 5.1.1 Underlying Data

For the setup of the model, real world data of a possible storage site in Western Germany was applied. The geometry of the aquifer top was provided in CAD data, which was processed with the CAD tool Rhino3D. It was used to create the aquifer geometry. With the software ICEM-CFD a hexahedral grid with  $48 \times 48 \times 20 = 46080$  nodes was generated. The node density in the vicinity of the well (center of the domain) is slightly higher than at the outer lying parts of the grid. Moreover, grid density decreases from bottom to the top of the aquifer, because the injection is situated at the bottom of the domain and the strongest gradients can be found there.

The examined part of the aquifer was delineated from a bigger geometry in order to receive reasonable boundaries and a smaller model domain which is better to handle. This sub domain should be representative for the larger domain. Therefore, the deepest part of the whole geometry was used, so that a preferably high  $\text{CO}_2$  density could be reached. Moreover, the domain with the strongest formation water flow was chosen. The whole domain and the examined sub domain, which is highlighted, are shown in figure 5.2. The green lines show the contours of the cap rock. Moreover, CAD data about groundwater isolines was available. The formation water isolines, which are shown in blue in figure 5.2, were used for the definition of the water pressure at the west and the east boundary (considering the orientation of the axes) and thus to generate the formation water flow from the west to east boundary of the domain.

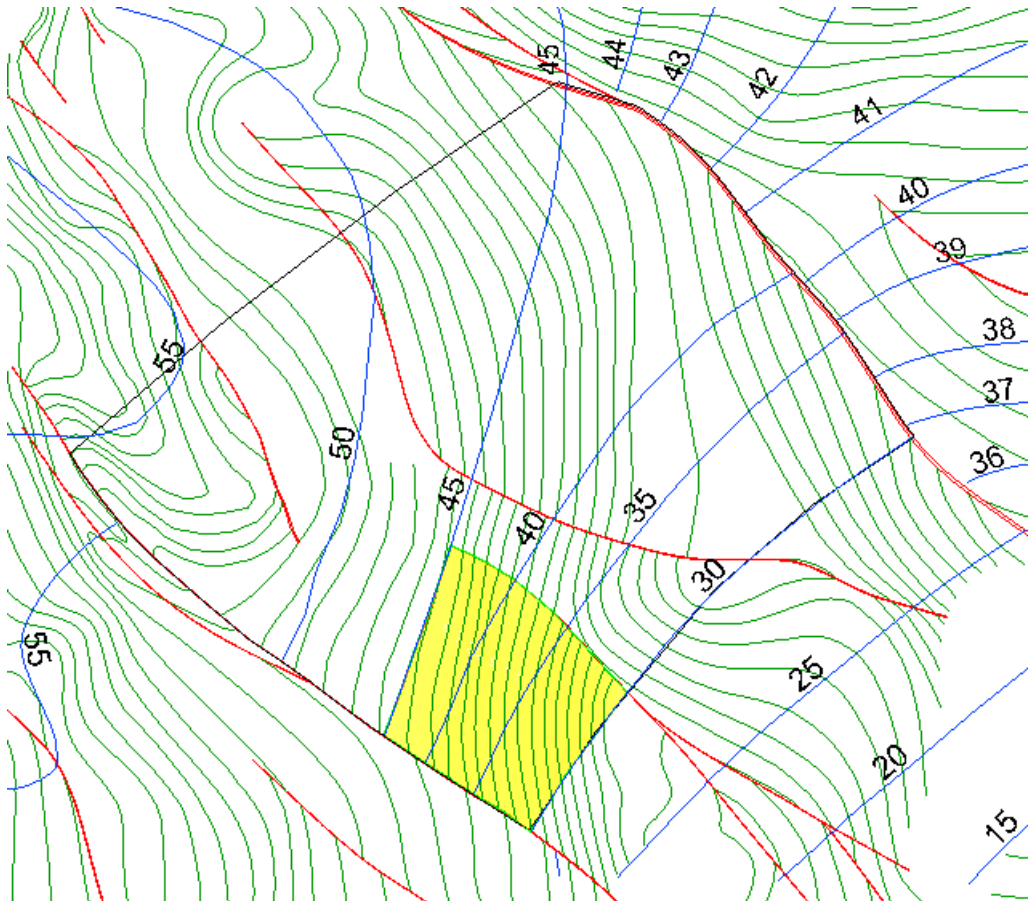


Figure 5.2: Top view on the whole domain. The part of the domain that was chosen for further examination is highlighted.

### 5.1.2 Boundary Conditions

The formation water isolines in the examined area are shown in figure 5.2. For model implementation, two no-flow boundaries in the north and south of the aquifer were set. The water pressure isolines are perpendicular to the boundary surfaces in the north, so no water flow across this boundary should take place in reality. The no-flow condition in the south of the domain was chosen along a fault. The isolines of the formation water indicate, that no flow takes place over this boundary. As already mentioned, the aquifer top and bottom were also set as impermeable Neumann boundaries.

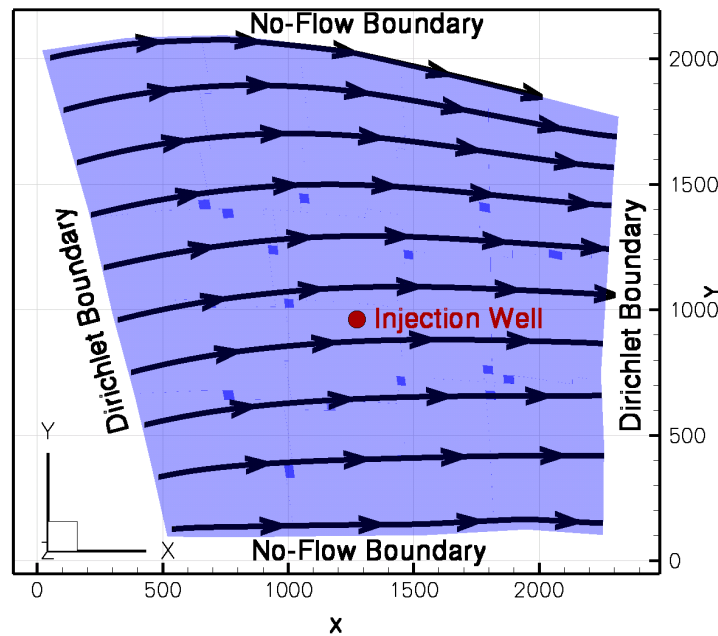


Figure 5.3: View on the top of the aquifer showing the stream traces of the undisturbed formation water flow and the boundary conditions at the sides of the domain.

The west and east boundaries are set as Dirichlet boundaries with the constant pressure taken from the water isolines. The pressure is approximately 1.5 bars higher at the west boundary than in the east, introducing a water flow from the west to the east boundary, downwards the aquifer. The model axes are oriented perpendicular to the model boundaries, with the X-axis pointing contrary to the predominant flow direction of the formation water. The side boundaries are depicted in figure 5.3.

For the injection well in the middle of the reservoir, a constant flux boundary was chosen. This was done by using the source and sink term of the mass balance,

introducing a constant mass flux into the system.

The temperature was defined as in the two-dimensional models by the geothermal gradient, which is 30 K/km. The injection temperature was set as the temperature that the aquifer has before the injection starts at the injection point.

### 5.1.3 Aquifer and Fluid Properties

The aquifer and fluid properties that are used here are the same as the ones that were used in the two-dimensional considerations. Table 5.1 gives an overview of the applied values:

Geothermal gradient [K/100m]	3
Porosity [-]	0.2
Anisotropy [-]	0.1
Salt content [Mass-%]	0.1

Table 5.1: Constant parameters of the 3D simulations

A rough distribution of the permeability and porosity within the aquifer was taken from maps, which were scanned and fitted to the model area. They showed that the porosity distribution within the examined part is roughly homogeneous, whereas the permeability varies between two ranges. First, an average permeability of  $1\text{E-}12\text{ m}^2$  was applied. This was later on changed to two different permeabilities, in order to see the effect of this. These two permeabilities were calculated as mean value of the corresponding ranges, that occurred in the maps.

The same capillary pressure - saturation relationship and relative permeability - saturation relationship after Brooks and Corey that were used for the two-dimensional models were also applied here. The parameters are depicted in table 5.2.

$S_{w,r}$ [-]	0.1
$S_{n,r}$ [-]	0.05
$p_D$ [Pa]	22000
$\lambda$ [-]	1.5

Table 5.2: Brooks-Corey parameters

## 5.2 Description of the Different Model Runs

Several model runs with different injection rates were performed. The CO<sub>2</sub> injection rate was varied in the different cases between 0.1 megatons per year and 2.3 megatons per year, which is in the range of the emissions of a medium sized coal plant. Then, the whole aquifer and injection point was moved 700 meters deeper in order to see, how the injected CO<sub>2</sub> would behave in a supercritical state of aggregation. In this case, an injection rate of 1 million tons per year was applied. In the last run, two zones with different permeabilities were inserted. An injection rate of 1 megatons per year was used again. An overview of these values is presented in table 5.3:

Case	Injection Rate [Mtons/a]	Depth of Injection [m b.s.l.]	Permeability
1	1	380	homogeneous
2	2.3	380	homogeneous
3	0.5	380	homogeneous
4	0.1	380	homogeneous
5	1	1080	homogeneous
6	1	380	two permeabilities

Table 5.3: Overview of simulated cases

With the help of these models it can be examined, how the injected CO<sub>2</sub> behaves in the respective circumstances. The following describes and shows the simulation outputs of the different cases.

### 5.2.1 Case 1: 1 Mtons per Year, Normal Depth

Since the aquifer has a high thickness of 250 meters and an anisotropy factor of 0.1, the injected CO<sub>2</sub> can first freely move through the aquifer. It takes 210 days, until the dipped cap rock is reached. The dominating force until then is first of advective origin and further away from the well more and more buoyancy driven. When the plume reaches the cap rock, it has to follow the contours of the aquifer top and it spreads out laterally at the cap rock in all directions. The same behavior could be recognized in the two-dimensional simulations. The buoyancy drives it up dip, whereas the ambient water flow is acting against this motion. In this case, the water flow shows little influence on the plume evolution.

Figure 5.11 shows the temporal development of the CO<sub>2</sub> saturation. The four pictures show the cross-section along the aquifer dip in the main water flow direction (positive X-direction) at different points in time. When the injection starts, the plume is of approximately elliptic shape. When it reaches the cap rock, the plume spreads there and the saturations at the cap rock increase. The main propagation is then directly under the cap rock in a thin zone. The influence of the water flow on the shape of

the plume can hardly be recognized. This indicates, that the pressure gradient at the injection well is higher than the gradient provided by the water flow.

Moreover, the formation water flow field was examined with the help of stream traces of the water phase. It showed, that with this injection rate, the injection affects the water flow so strong, that the flow direction in the upstream part of the aquifer is inverted. The water flows out of the aquifer at both Dirichlet boundaries. Two exemplary views on the top of the aquifer with the corresponding water stream traces are shown in figure 5.4. On the right side, a lower injection rate of 0.1 Mtons/year was applied (case 4). The formation water dodges around the injection well, but does not change the direction.

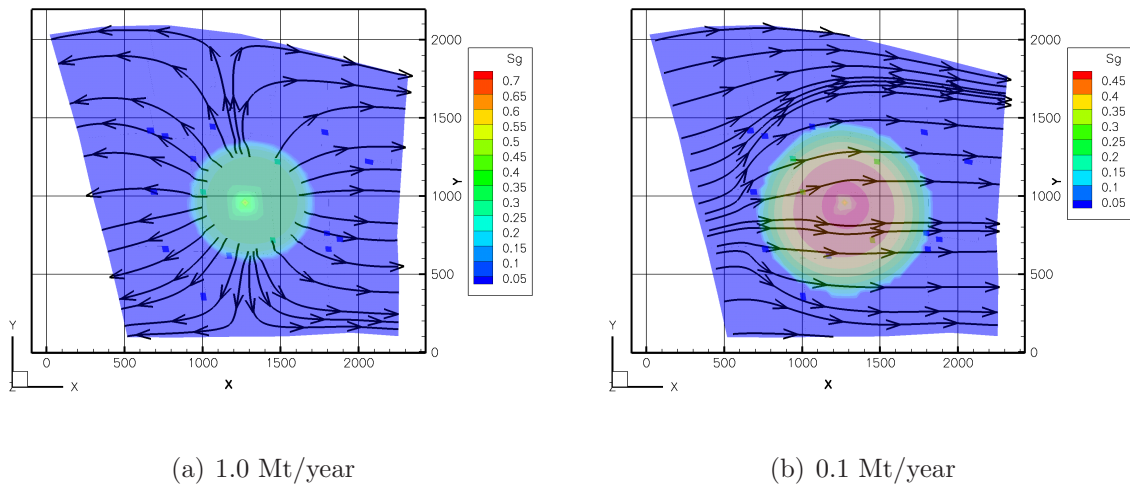


Figure 5.4: Stream traces of the formation water from top view with an injection rate of 1 Mt/yr in figure (a) and with 0.1 Mt/yr in figure (b).

### 5.2.2 Case 2: 2.3 Mtons per Year, Normal Depth

This is the injection rate, which is planned in order to sequestrate all of the separated  $\text{CO}_2$ , which is produced in a coal plant. Arising pressure gradients at the injection well are even higher than in the first case, and the evolving plume creates strong advective forces. These forces have a dominant influence on the flow field and on the shape of the plume. The influence of the ambient water flow is almost negligible in this case. The plume spreads out into all directions, and the model boundaries are reached already after less than one year of injection. Such a high injection rate is not suitable for the given aquifer.

### 5.2.3 Case 3: 0.5 Mtons per Year, Normal Depth

This case has an injection rate between case 1 and case 3. It is used in the following to compare the dissolution behavior with Case 4 when the injection is turned off.

### 5.2.4 Case 4: 0.1 Mtons per Year, Normal Depth

In this case, the  $\text{CO}_2$  is injected with a low injection rate of 0.1 million tons per year into the aquifer. Now it takes much longer, until the cap rock and later on the model boundaries are reached. In this case, it took 630 days to reach the cap rock. The plume has a different shape, since the evolving pressure gradients are lower and the influence of buoyancy is stronger. The corresponding saturation profile is shown in figure 5.5. The maximum saturation, that can be found in this case is far lower than in the case 1. It amounts to 0.45 instead of 0.8.

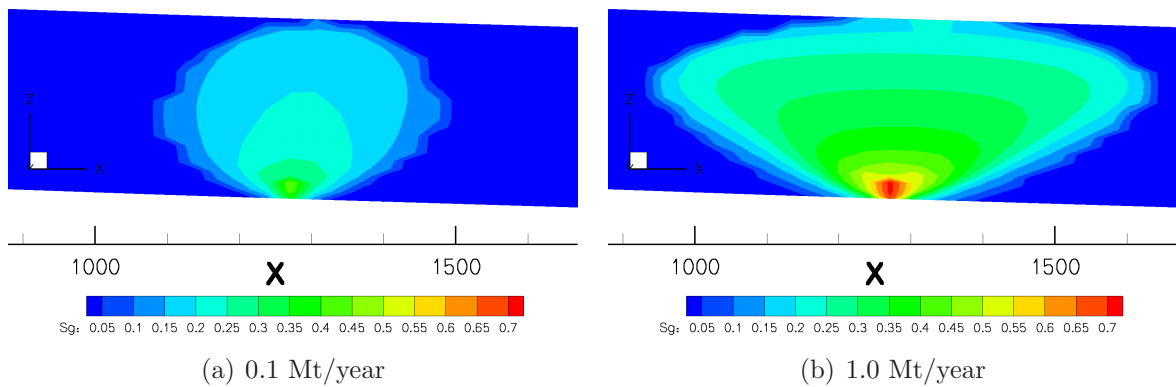


Figure 5.5: Saturation profile when the cap rock is reached for case 1 (after 210d) and Case 4 (after 630d)

Four exemplary saturation profiles at different points in time can be found at the end of this chapter in figure 5.12.

### 5.2.5 Case 5: 1 Mtons per Year in a Supercritical State

The considered aquifer is then placed 700 meters deeper than in the other cases. This changes the state of aggregation of the carbon dioxide phase to supercritical, resulting in a much higher density and viscosity. The resulting propagation behavior is different to other runs in lower depths. The plume has a lower tendency to rise upwards. Moreover, the plume has the strongest shift in downwards direction of all runs. It takes more time until the cap rock is reached than in the other considered cases. It is reached after more than 830 days. Several saturation profiles can be found at the end of this chapter in figure 5.13.

### 5.2.6 Case 6: Two Different Permeability Zones

In this model run, the domain was subdivided at  $Y = 810\text{m}$  into two sub domains with different permeabilities, one with a permeability of  $1.63\text{E-}12 \text{ m}^2$  (K2) and the other with  $0.51\text{E-}12$  (K1). These are the average group values, that could be taken out of maps. The injection well is situated in the lower permeable part in the south of the domain. This is depicted in figure 5.6

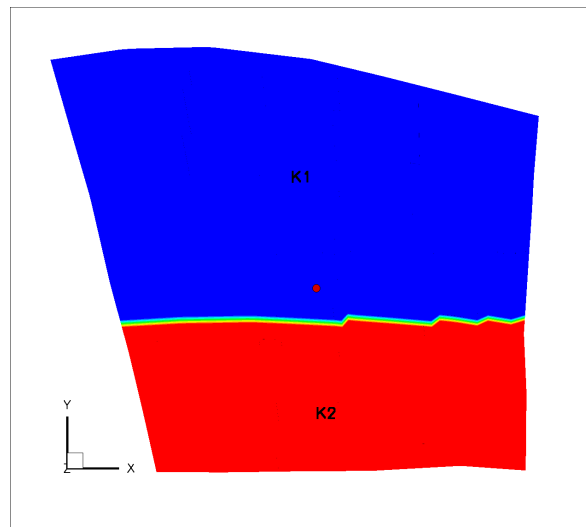


Figure 5.6: Top View on the Aquifer, Showing the Permeability Distribution Within the Aquifer.

At first, the plume behaves similar to the other cases. But when the boundary to the higher permeable zone is reached, the following  $\text{CO}_2$  is attracted in this direction. The plume is developing faster in this zone, then. Moreover, higher phase velocities of the carbon dioxide can be observed there.

Figure 5.7 shows the saturation at a cross-section perpendicular to the groundwater flow and the permeability zones. The small arrows indicate the velocity field. Although the permeability distribution will probably not have that sharp front in reality, this simulation run shows the principal behavior, when the plume reaches a zone with a higher permeability. It also shows the influence of buoyancy flow considering different permeabilities: In the lower permeable zone, the  $\text{CO}_2$  phase is migrating faster upwards than in the lower permeable zone.

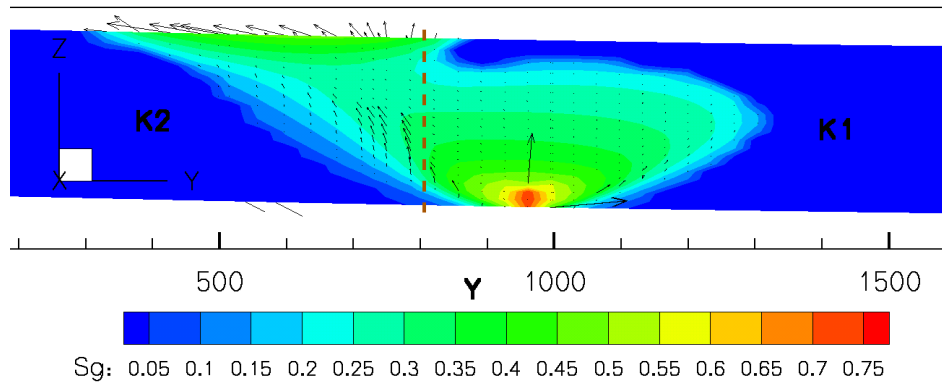


Figure 5.7: Slice view in Y-direction using two different permeabilities. The dashed line shows the border of the two permeability zones. K1 indicates the lower permeable and K2 the higher permeable zone. The plume develops preferably in the higher permeable zone. The arrows indicate the velocity of the CO<sub>2</sub> phase.

## 5.3 After the Injection is Turned off

### 5.3.1 Behavior After the Injection is Turned off

In case 4 with an injection rate of 0.1 million tons per year in a shallow depth, it is interesting to see what happens when the injection is stopped before the aquifer reaches the boundaries. Therefore, the injection was turned off after eight years of constant injection. Figure 5.8 shows the saturation profile in flow direction at the moment when the injection is switched off and 0.8 million tons of CO<sub>2</sub> are in the aquifer. The second picture depicts the saturation eight years later. One can see that the plume stops migrating upwards. It remains in place at first.

The pressure distribution within the aquifer abruptly changes, when the injection is stopped. The influence of the injection on the pressure field is turned off. The major part of the CO<sub>2</sub> dissolves or is at residual saturation then. The highest CO<sub>2</sub> saturations can be found directly under the cap rock. This indicates, that the mobile part of the plume within the aquifer continues moving to the cap rock. The formation water flow in down dip direction slowly takes the plume and the dissolved CO<sub>2</sub> with it. This process may take quite long due to a very slow water flow velocity of 1E-7 m/s.

The injection was also stopped for case 1 and the further plume development was observed. But it appears, that the amount of CO<sub>2</sub> in phase is that much, that it continues to rise upwards and it forces the plume to spread in both directions along the cap rock. The model boundaries are reached, soon. This is due to the before mentioned higher saturations, that occur here. The CO<sub>2</sub> in phase remains mobile for a longer time than in the case with a lower injection rate.

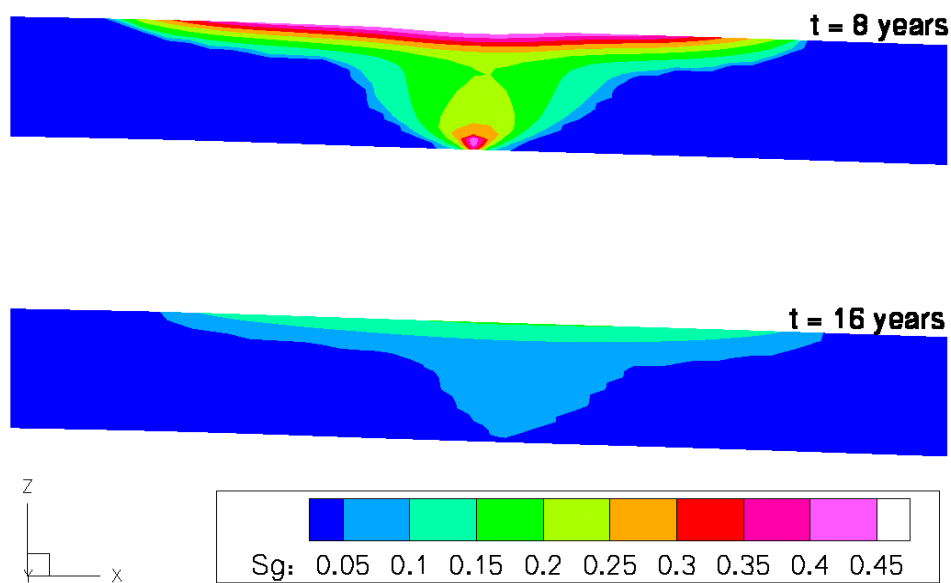


Figure 5.8: Slice view into the middle of the reservoir after stopping the injection. The first image shows the saturation profile after stopping the injection after 8 years of injecting 0.1 Mt/year. The second image shows the saturation profile 8 years later. A great part of the injected  $\text{CO}_2$  has dissolved in the formation brine and the saturations are almost at residual saturation. The highest saturation can be found directly at the cap rock.

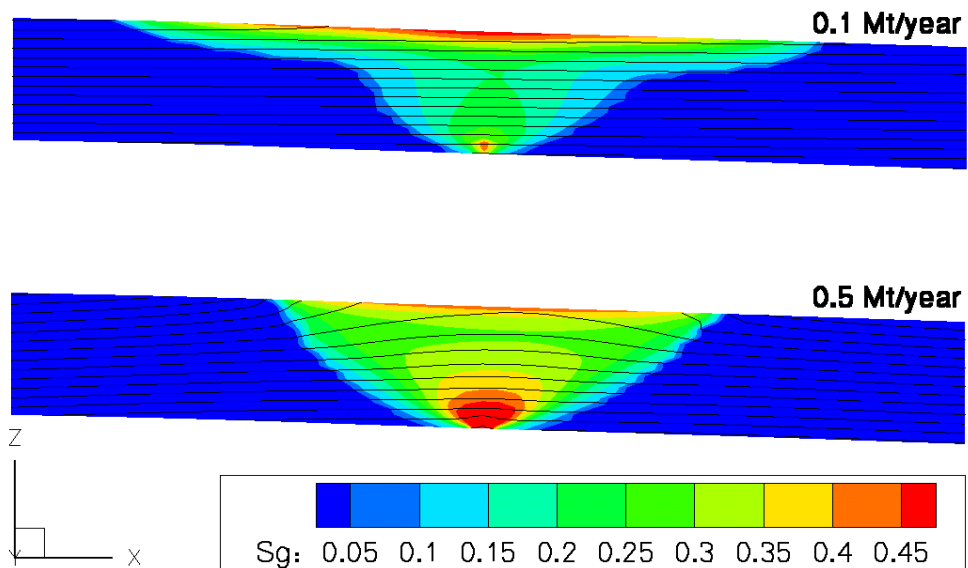


Figure 5.9: Saturation profile with 0.8 Mt injected CO<sub>2</sub> in the system, after 8 years with 0.1 t/a injection rate and after 1.6 years with 0.5 t/a. Moreover, the pressure isolines are depicted.

Picture 5.9 shows a comparison of the saturations of case 3 (0.1 Mt/year) and case 4 (0.5 Mt/year) with the same CO<sub>2</sub> mass injected within different time periods into the system. In case 3 it takes eight years to inject 0.8 Mtons of CO<sub>2</sub>, in case 4 it takes only 1.6 years due to the higher injection rate. The resulting plots clearly show, that in the case of a higher injection rate the system is more dominated by viscous forces and the plume spreads more into the aquifer. In the first picture, the CO<sub>2</sub> is injected slowly. It does not spread that far but rises upwards to the cap rock. When it reaches there, it spreads in all directions along the impermeable layer. Thereby, lower saturation values are reached within the aquifer. When the injection is turned off then, the major part is already at the cap rock and does not move further upwards. Residual saturations and therewith an immobile state are reached soon.

With a higher injection rate of 0.5 Mt per year, this behaves differently. The plume spreads further into the aquifer, before reaching the cap rock. After the injection is turned off, a great part of the CO<sub>2</sub> within the aquifer is still mobile and continues to move to the cap rock and spread there. Buoyancy is then dominating the motion of the plume. Moreover, the model boundaries are reached and the CO<sub>2</sub> is flowing out of the system, due to the spreading of the plume. This was the reason, why the cases with higher injection rates could not be examined. When the injection was turned off in these cases, the saturations in the aquifer were even higher and a strong buoyancy flow could be observed. This rose up to the cap rock and spread laterally, until the boundary was reached. Since the boundaries have a big influence on the flow behavior from thereon, these cases were not examined further.

However, the volume that was in contact with CO<sub>2</sub> before is larger than in the case with a lower injection rate. Thus, more CO<sub>2</sub> can be residually trapped within the aquifer.

### 5.3.1.1 Re-Injection

Since drilling and well constructing costs are high, it would be economically interesting to inject after a certain time period into the same aquifer again, so that the bore hole and the equipment could be used again. Therefore, the injection was turned on again for case 2 (0.1 Mt/a) after eight years of recovery. In this case, the effect of hysteresis (explained in chapter 2) should be taken into account for more accurate results. This was not made here since this would exceed the scope of the thesis. Here, only the principal behavior of re-injection shall be examined.

The output of the model run shows, that the newly injected CO<sub>2</sub> preferably follows the residual saturations of the last injection. This is mainly due to the effect of relative permeability. High saturations and thus a good relative permeability are reached sooner in the presaturated domains. Since the old plume has moved little in downwards direction, the new plume that arises is shifted about 50 meters down dip. The same saturations are reached again after less than two years of injection.

### 5.3.1.2 Dissolution Behavior

In general, during the injection the dissolved part of the injected amount of carbon dioxide is relatively constant and depending mainly on temperature and pressure. In the models, no dissolution kinetics are implemented. The carbon dioxide is dissolved immediately to a certain part, that is determined by the solubility function. Subsequently, the share of dissolved CO<sub>2</sub> is almost constant. Moreover, the values for the share of dissolved CO<sub>2</sub> of the total injected mass change with different injection rates. This is mainly due to the occurring higher pressure differences and a larger contact volume of the plume with the surrounding brine, which increase the solubility.

In the case 4, the dissolution behavior is examined further. It is depicted in figure 5.10. It includes three different stages: First, a constant mass flow into the system was applied, which was switched off after 8 years of injection. After switching the injection off, the CO<sub>2</sub> within the system is more and more dissolved. One can see, that with the low injection rate of 0.1 Mt per year the major part of the carbon dioxide is being dissolved in the formation brine. This was up to 90 per cent of the injected amount. It can then be transported away with the ambient water flow. Due to low flow velocities, this takes very long.

Then, 8 years later, the injection was switched on again. This is also reflected in figure 5.10. The simulations was stopped, when the same amount of CO<sub>2</sub> in phase was reached.

## 5.4 Not Examined Parts and Risks

Here, fingering shall be mentioned as possible risk. Fingering may occur, when density and viscosity differences of two fluids are significantly high, which is the case when CO<sub>2</sub> is sequestered into a shallow depth. Fingering is the formation of finger-like protuberances in the propagation front. An explanation can be found in Homsy [9]. These fingers are then preferred flow paths for the following fluid and lead to a instability of the propagation front. Moreover, the behavior of these 'fingers' and subsequently the propagation behavior of the CO<sub>2</sub> plume is difficult to predict. To get an idea, if fingering might occur, several estimations exist. To give an example, the mobility ratio shall be mentioned. It can be used to make an estimation, whether fingers form at the front or a stable displacement occurs. The mobility ratio is defined as

$$M = \frac{\mu_w \cdot k_{r,n}}{\mu_n \cdot k_{r,w}}. \quad (5.1)$$

When this ratio is smaller than one, stable displacement should occur. When it becomes bigger than one, the risk of fingering is high. In order to get an impression, in which range we are dealing, following values corresponding to a depth of 400 meters are inserted into the mobility ratio:

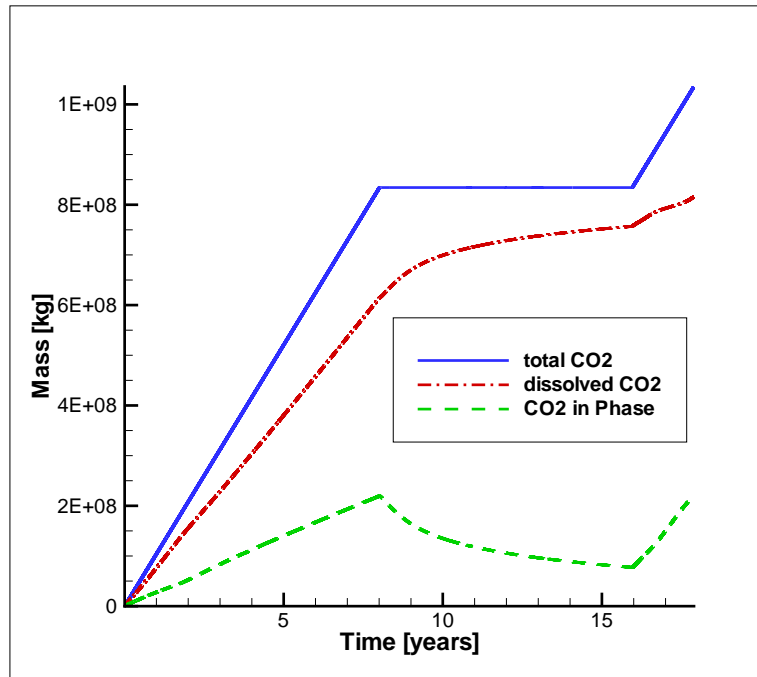


Figure 5.10: Graph with the ratio of dissolved CO<sub>2</sub> to the total injected CO<sub>2</sub>, including 3 different phases: 8 years injection of 0.1 Mt/year, 8 years of recreation without injection and then a re-injection.

- brine viscosity: 1.1E-3
- CO<sub>2</sub> viscosity: 1.6E-5

For this rough estimation, the same relative permeability is used, leading to a mobility ratio of 69. This indicates, that fingering is likely to occur and has to be examined further.

Another issue is that fractures and faults can be found in the direct surrounding of the aquifer, which should be considered further. Especially the faults might pose a problem for secure CO<sub>2</sub> storage. In the vicinity of the examined area, these faults are up to 30 meters in vertical direction. They might provide a possible leakage path for the CO<sub>2</sub>. The used model domain was cut directly at a fault. The model runs were stopped, before this fault was reached.

The entry behavior at the cap rock is also an issue, which should be examined further. Since the CO<sub>2</sub> is in a gaseous state and has a low viscosity, the risk of an escape through small fractures has to be considered. Moreover, the long-term behavior of the injected CO<sub>2</sub> has to be examined, in order to get an idea of the ongoing diffusion processes, which happen over a long time period and are beyond the scope of this thesis.

Furthermore, the friction forces at the interface of the phases are not taken into account in the performed simulations. Potentially, they could positively influence the plume evolution in down dip direction.

## 5.5 Chances and Possibilities

The simulations show, that the examined site may be suitable for CO<sub>2</sub> storage. An issue is its shallow depth, which results in a gaseous phase state of the CO<sub>2</sub> and consequently in very high buoyancy forces. This strengthens the probability of a possible escape of the CO<sub>2</sub> through the cap rock. Moreover, gaseous CO<sub>2</sub> needs much more space for the same injected mass. The density in the simulated supercritical case was up to ten times higher than in the subcritical ones. Thus, a very large aquifer would be needed in order to store the carbon dioxide, that is emitted by an average coal plant.

During the injection, the advective forces of the formation water flow are in all considered cases too weak to drive the CO<sub>2</sub> phase in down dip direction (especially with high injection rates), although they have a certain influence on the propagation behavior. The shape of the CO<sub>2</sub> plume is deformed by the forces that arise from the water flow. The intensity of this deformation clearly depends on the injection rate of the CO<sub>2</sub>. As could be seen before, the water flow direction can even be inverted, if high injection rates are applied.

An injection of 2.3 Million tons per year in this site is not possible over a long period. The aquifer capacity is too small with the low density of the CO<sub>2</sub>. Sequestration over several years would be possible if the CO<sub>2</sub> phase was in a supercritical state.

A possibility for CO<sub>2</sub> storage would be to apply an injection rate, where the major part of the injected CO<sub>2</sub> is being solved in the brine when the injection is turned off. This could be observed in case 4 with an injection rate of 0.1 Mtons/year. But these injection rates might be too small, so that this option would become uneconomically. At least, several different wells would be required in order to sequester the foreseen amount, maybe with an alternation of storage sites.

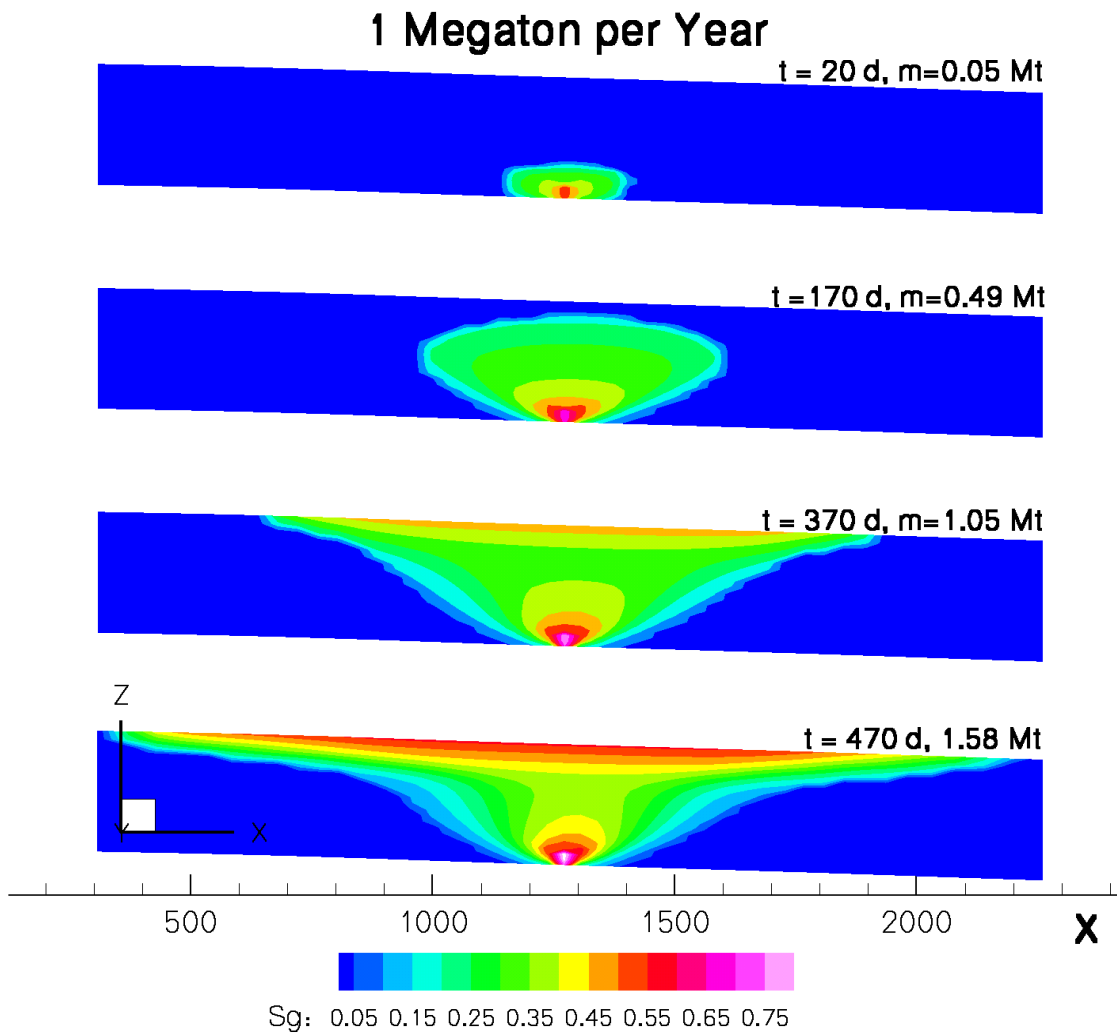


Figure 5.11: Slice view into the middle of the reservoir in case 1 (1 Mt/year). The saturation distribution along the dip and groundwater flow at different times are shown.

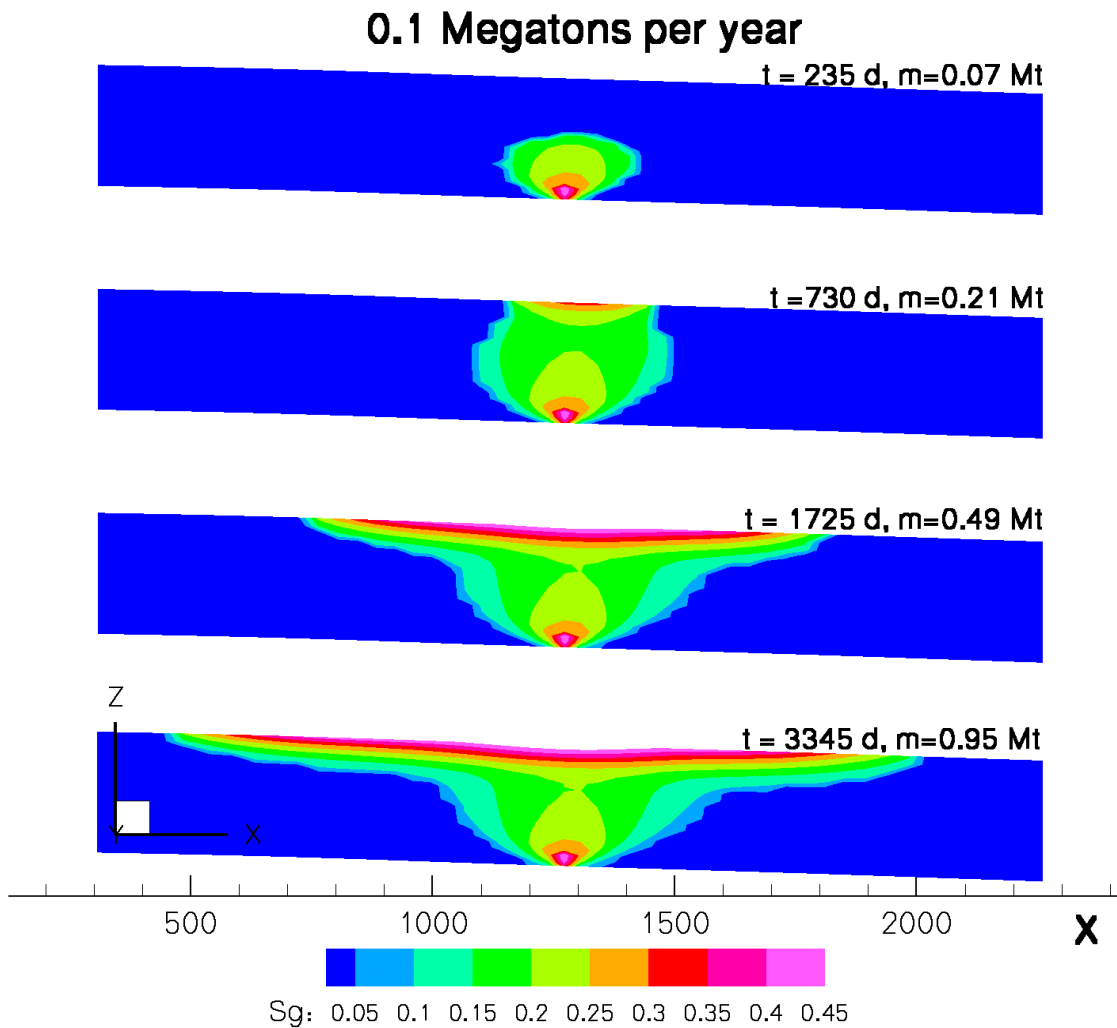


Figure 5.12: Slice view into the middle of the reservoir in case 4 (0.1 Mt/year). The saturation distribution along the dip and formation water flow at different times are shown.

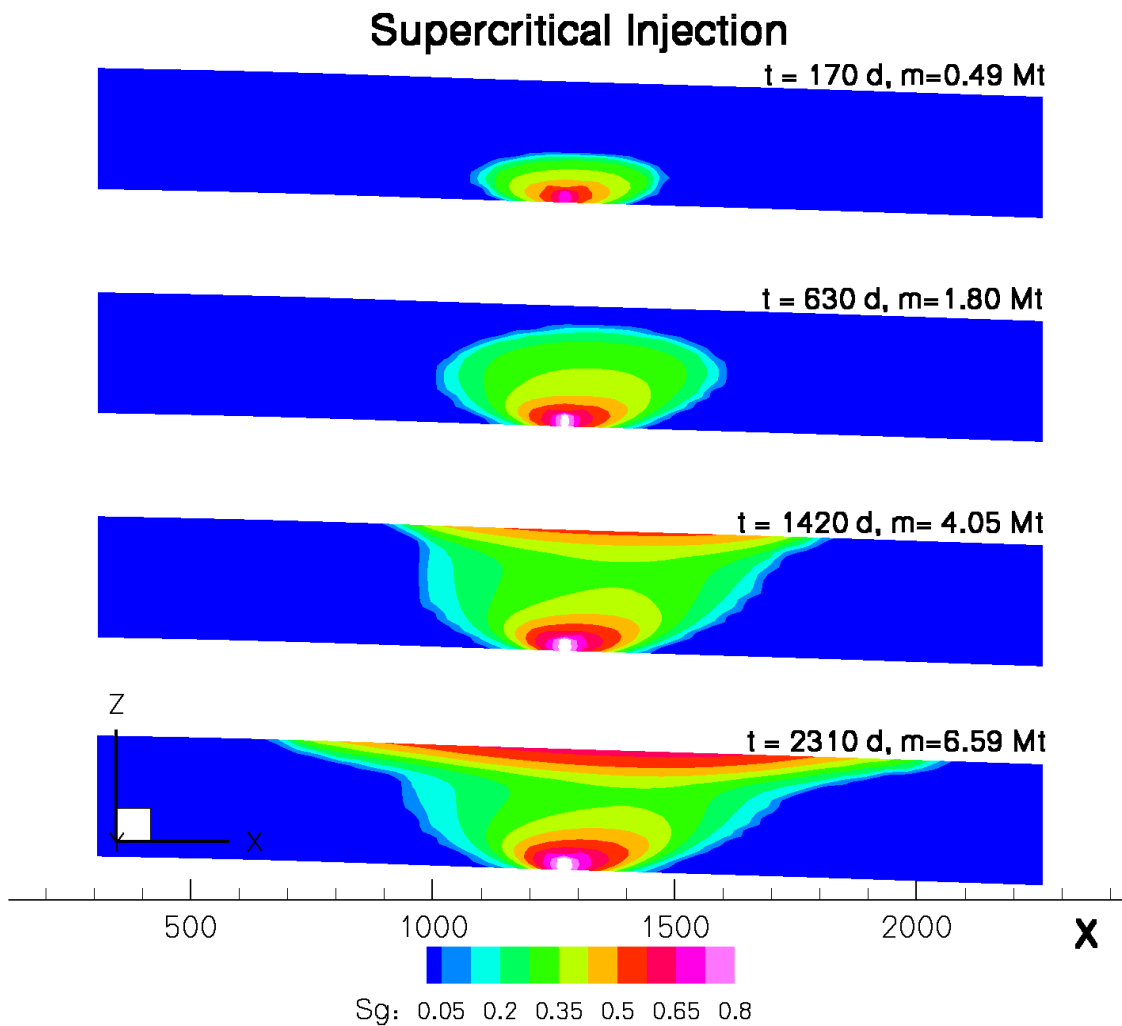


Figure 5.13: Slice view into the middle of the reservoir in case 5 (supercritical injection). The injection place is situated at a depth of more than 1000 meters, leading to a supercritical state and a different propagation behavior. The saturation distribution along the dip and groundwater flow at different times is depicted.

# Chapter 6

## Summary and Outlook

### 6.1 Conclusions and Outlook

The two-dimensional simulations showed the principal behavior of a CO<sub>2</sub> plume within a dipped aquifer including a groundwater flow in down dip direction. This process revealed to be very complex. The influencing parameters are highly non-linear. Different parameters were varied and their influence qualitatively examined.

The derived pressure number showed to be useful for an estimation of the main flow direction of the plume. The Van-Lookeren number, which was used as a gravity number to characterize the ratio of buoyancy forces to viscous forces, showed an unexpected behavior, when CO<sub>2</sub> is injected into a shallow depth. It showed, that the influence of the viscous forces increase even more than the buoyancy forces, when the injection depth is becoming less. Possible reasons were briefly discussed, namely a higher velocity and the lower density of CO<sub>2</sub>. Moreover, the Van-Lookeren number was successfully used to describe the influence of the viscous and buoyancy forces.

Furthermore, the consideration of dimensionless numbers showed, that for the scaling of this complex process at least several different numbers are needed. To get an impression of the behavior of the injected CO<sub>2</sub>, several restricting assumptions had to be made, and the results cannot be generalized. For example, the pressure ratio, which delivered good results in estimating the preferred flow direction in two-dimensional models could not be transferred to the three-dimensional space since the evolving pressure field in 3D is much more complex. The simplifying assumptions, that were made for the 2D models could not be applied here. Further investigations in three-dimensional space have to be made. Moreover, this shows the need for numerical models, which are capable of taking the main processes into account.

The three-dimensional examination of a real-world site showed, that storage in shallow depths is in principal possible but contains several risks and implications. Buoyancy forces are much stronger, which increases the risk of a CO<sub>2</sub> leakage. The

occurring propagation velocity is faster than in deep aquifers. More space is needed to store the same amount of carbon dioxide. In order to obtain a comparable mass flow rate, a much higher injection pressure is needed in a subcritical case than in a supercritical case. Consequently, the storage into deep aquifers should be preferred.

# Bibliography

- [1] Ansolabehere, S. et al. *The future of coal - Options for a carbon-constrained world*. 2007.
- [2] Arbeitsgemeinschaft Energiebilanzen. *Primärenergie 2006*. 2007.
- [3] Bacchu, S. and Bennion, B. Relative permeability characteristics for supercritical CO<sub>2</sub> displacing water in a variety of potential sequestration zones in the Western Canada Sedimentary Basin. *SPE 95547*, 2005.
- [4] Bielinski, A. *Numerical simulation of CO<sub>2</sub> sequestration in geological formations*. Dissertation, Institut für Wasserbau, Universität Stuttgart, 2007.
- [5] Class, H.; Helmig, R. and Bastian, P. *Numerical simulation of nonisothermal multiphase multicomponent processes in porous media - 1. An efficient solution technique*. 2001.
- [6] Duan, Z. and Sun, R. An improved model calculating CO<sub>2</sub> solubility in pure water and aqueous NaCl solutions from 273 to 533 K and from 0 to 2000 bar. *Chemical Geology*, 193:257–271, 2003.
- [7] Helmig, R. *Multiphase flow and transport processes in the subsurface: A contribution to the modeling of hydrosystems*. Springer Verlag, 1997.
- [8] Helmig, R.; Class, H.; Huber, R.; Sheta, H.; Ewing, J.; Hinkelmann, R.; Jakobs, H. and Bastian, P. Architecture of the modular program system MUFTE-UG for simulating multiphase flow and transport processes in heterogeneous porous media. *Mathematische Geologie*, 1998.
- [9] Homsy, G. Viscous fingering in porous media. *Annual Reviews Fluid Mechanics*, 19:271–311, 1987.
- [10] Huber, R. U. *Compositional multiphase flow and transport in heterogeneous porous media*. Dissertation, Institut für Wasserbau, Universität Stuttgart, 1999.
- [11] Kopp, A. *Research proposal "Sensitivity analysis of CO<sub>2</sub> injection processes in geologic formations"*. 2007.
- [12] Lookeren, J. v. Calculation methods for linear and radial steam flow in oil reservoirs. *SPE 6788*, S. 427–439, 1983.

- 
- [13] Shook, M.; Li, D. and Lake, L. W. Scaling immiscible flow through permeable media by inspectional analysis. *In Situ*, 16(4):311–349, 1992.
- [14] Span, R. and Wagner, W. A new equation of state for carbon dioxide covering the fluid Region from the triple-point temperature to 1100 K at pressures up to 800 MPa. *J. Phys. Chem. Ref. Data*, 25(6):1509–1596, 1996.
- [15] UN Intergovernmental Panel on Climate Change (IPCC). *Climate change 2007, 4th Assessment Report*. 2007.